Effect of helium and silver ions co-implanted into polycrystalline silicon carbide at 350 ºC on structural evolution and migration behaviour of silver

by

Sive Zizo Mtsi

Submitted in partial fulfilment of the requirements for the degree

Master of Science (MSc) in Physics

In the Faculty of Natural and Agricultural Science

University of Pretoria

Pretoria

February 2022

Supervisor: Prof T.T. Hlatshwayo

DECLARATION OF ORIGINALITY

I, Sive Zizo Mtsi, declare that the dissertation, which I hereby submit for the degree of MSc in Physics at the University of Pretoria, is my own work and has not previously been submitted by me for a degree at this or any other tertiary university.

Signature ………………..

Date ……………………..

Summary

Effect of helium and silver ions co-implanted into polycrystalline silicon carbide at 350 ºC of structural evolution and migration behaviour of silver

by

SIVE ZIZO MTSI

Submitted in partial fulfilment of the requirements for the degree of MSc in Physics in the Faculty of Natural and Agricultural Science, University of Pretoria

Supervisor: Prof T.T. Hlatshwayo

Safety of nuclear reactors strongly depends on the containment of fission products. In modern nuclear reactors, this is accomplished by coating the fuel with chemical vapour-deposited layers of carbon (C) and silicon carbide (SiC), in which SiC is the main barrier of fission products. During operation, at elevated temperatures, the SiC layer is subjected to various radiation in the presence of helium (He). Silver (Ag) is one of the fission products that is released by the coated fuel during operation, while He is known to form bubbles in SiC. These bubbles compromise the integrity of SiC as the main barrier of fission products. Hence, the effect of He bubbles in the migration of radiological important fission products needs to be understood.

In this study, the effect of helium (He) and silver (Ag) ions co-implanted into polycrystalline silicon carbide at 350 °C on structural evolution and migration behaviour of silver was investigated. Ag ions of 360 keV were implanted into polycrystalline SiC to a fluence of 2×10^{16} cm^{-2} at 350 °C. Some of the implanted samples were then implanted with He ions of 17 keV to a fluence of 1×10^{17} cm^{-2} also at 350 °C. Both Ag and co-implanted samples were then isochronally annealed at temperatures varying from 1000 °C to 1300 °C in steps of 100 °C for 5 hours.

The structural changes were characterized using Raman spectroscopy while morphological and topographical evolutions were characterized by scanning electron microscopy (SEM) and atomic force microscopy (AFM). The elemental depth profiles and concentration of implants

in as-implanted and annealed samples were monitored by heavy-ion elastic detection analysis (ERDA).

Both individual and co-implantation retained some defects in SiC without amorphization. These retained defects were slightly more in the co-implanted samples. Annealing of samples resulted in the progressive healing of defects in SiC. Co-implantation of He resulted in the formation of blisters and some holes on the SiC surface indicating the formation of He bubbles accompanied by some exfoliation of bubbles. The exfoliation increased with annealing temperature. These holes increased in number with annealing temperature resulting in the decrease in number of blisters. The formation of He bubbles and holes in the co-implanted samples caused the migration of Ag towards the surface accompanied by the loss of both Ag He. Annealing at 1100 ℃ caused loss of He accompanied by neither further migration nor loss of implanted Ag. No migration of Ag was observed in the Ag implanted samples annealed at 1100 ℃. Therefore, the formation of He bubbles enhanced the migration of Ag while cavities trap Ag implanted into SiC.

Acknowledgements

Table of Contents

List of figures

CHAPTER 1

INTRODUCTION

As the world population grows, the global energy demand is constantly rising [1]. The growing human population would lead to an energy crisis as the need for power supply surpasses electricity production. An increase in industrial activities and technological advances also play a role in this energy crisis [2]. Presently, fossil fuels account for 80% of global energy demand [3]. Fossil fuels' limited availability, exhaustible nature, and negative environmental impact make fossil fuels unsustainable. Fossil fuel combustion produces greenhouse gases, which lead to pollution, global warming and climate change, hence deterioration of human health [1, 4]. There is, therefore, a necessity to explore alternative energy sources that are clean and sustainable. Renewable and nuclear energy are arguably clean and sustainable energy sources with a minimal negative impact to the environment. Renewable energy comes from naturally occurring sources of energy. The primary types of renewable energy include solar, wind, hydro, geothermal, and biomass [5].

Solar power makes use of the radiation from the sun, which is transformed into electricity or heat by the use of solar technologies. Since atmospheric molecules and dust scatter solar radiation, not all radiation will reach the earth. Clouds also scatter solar radiation and reduce the concentration of radiation on earth [6, 7]. So when it is cloudy or raining, the efficiency of the solar energy system is reduced. Due to solar energy's reliance on sunlight, it won't generate power at night [8]. Solar energy is environmentally friendly, but its geographical and environmental dependence makes it an unsustainable form of energy. Wind power produces energy/electricity using the wind or air flows that occurs naturally in the atmosphere [9]. In modern wind turbines, the wind`s kinetic energy is captured and used to generate electricity. The natural currents of air spin the turbine, resulting in mechanical power, which is converted into electricity using a generator [10]. The main drawbacks of wind energy are fluctuating and undependable wind speeds. Very high wind speeds can result in wind turbines shutting and ceasing electricity generation, while inadequate speeds result in wind turbines not having enough power to generate current [9]. Wind power outages result in wind farms being unable to generate stable base-load power. Thus, to atone for losses of wind and outages, the

combination of wind farms is required to increase its capacities [11]. So this requires large amounts of land that can be used for agricultural purposes, as wind farms are usually built in rural areas. Also, wind power's dependency on weather makes it unsuitable to be the primary power source. Hydroelectric energy is a type of energy that is generated from flowing water. Potential energy is converted to kinetic energy as the flowing water flows through the turbine to generate electricity [12]. A geographic area's precipitation determines the amount of water available for producing hydropower. Electricity production can be adversely affected by seasonal variations and long-term changes in precipitation patterns, such as drought [13]. Hydro plants are created by damming a running water source. This effect means that whatever habitat was in that location is disturbed, thus ruining the river's ecosystem and environment [14].

Nuclear energy refers to the energy stored inside the nucleus of an atom. This energy can be used to generate electricity but must be released first. An atom releases energy through nuclear fission or fusion reaction [15]. A fission reaction occurs when a neutron collides with a heavy target nucleus, splitting it into two daughter nuclei called fission fragments, along with the release of energy in the form of heat and fast neutrons [16]. The fission of ^{235}U emits three neutrons as well to two daughter nuclei. If those emitted neutrons collide with neighbouring ^{235}U nuclei, they can trigger the nuclear fission of those atoms and instigate a self-sustaining nuclear chain reaction [17]. These controlled chain reactions generate both large quantities of thermal energy and neutrons [18]. The main detrimental consequence of the fission reaction is radioactive fission products. Nuclear reactors do not generate carbon emissions, but there are concerns about the potential risks associated with the accidental release of these radioactive fission products. Reactor overheating can cause the melting of nuclear fuel and the containment system of the reactor vessel. Loss of containment can release large amounts of harmful radiation into the environment [18]. The revival of nuclear reactors as a clean energy source requires a clear demonstration of reactor's safety during operation and in the event of an accident.

Modern high-temperature reactors are capable of operating at extremely high temperatures. An efficient cooling system of the core and high-temperature resistance fuel particles prevent overheating. The particle's thermal resistance creates an upper bound inherently in temperature control [19]. In the pebble bed modular reactor (PBMR), a modern high-temperature gas-cooled reactor (HTGR), safety is improved by coating the fuel particle with four chemical vapor deposited (CVD) layers. The coating layers allow the fuel particle to operate as its

containment system by retaining fission products under all reactor conditions [20]. In a TRISO particle, the nuclear fuel is composed of uranium dioxide (UO_2) coated by CVD layers. The first coating layer is a porous carbon buffer. This layer reduces recoiling fission products (FPs) and accommodates internal gas accumulation. The other three layers are the inner pyrolytic carbon (IPyC) layer, a silicon carbide (SiC) layer, and an outer pyrolytic carbon (OPyC) layer as shown in figure 1.1. The inner pyrolytic carbon layer acts as a diffusion barrier to most non-metallic FPs. IPyC also stops corrosive chemicals and by-products of the deposition of the SiC layer from entering and reacting with the uranium in the kernel. Silicon carbide layer acts as the main diffusion barrier of fission products. While the outer pyrolytic carbon layer protects the SiC layer from mechanical deterioration and external chemical reactions. Additionally, OPyC prevents the TRISO particle from rupturing completely under mechanical shock and releasing the radioactive fission products held inside it [20].
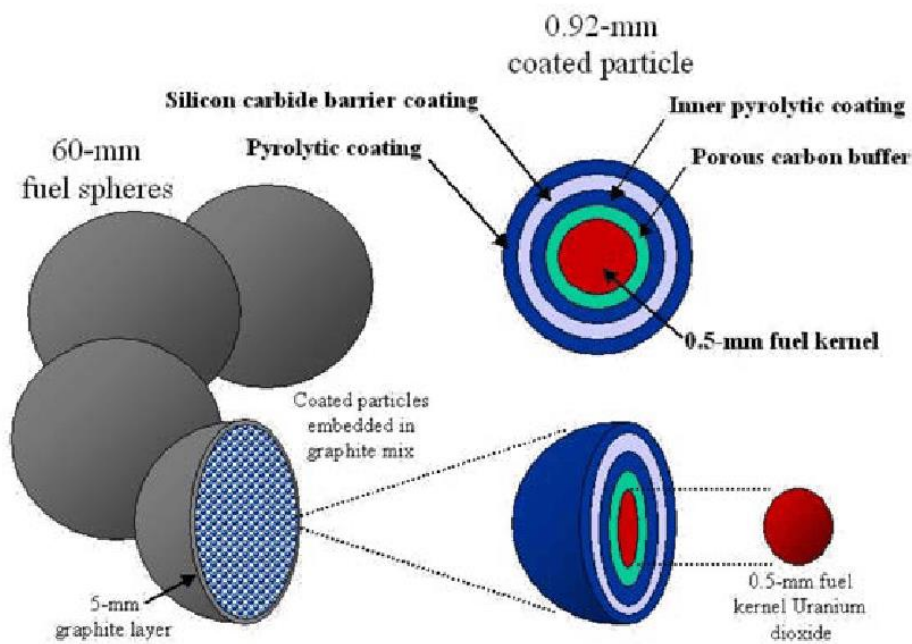
Figure 1. 1: Schematic diagram of a fuel particle of the PBMR and a cross-section of High temperature reactor (HTR), pebble [21].

SiC is a material whose physical and chemical properties make it appropriate to use in a nuclear environment. The inertness of SiC enables it to withstand chemical attacks, thus making it a high corrosion resistance material [20, 22]. A distance of 1.89 Å between Si and C results in a high bond strength which hardens the material. The Mohs hardness of approximately 9.5 gives

SiC a great strength and durability to be structural support for the TRISO-coated fuel particle [23]. This material provides exceptional thermal shock resistance due to its high thermal conductivity coupled with low thermal expansion and high strength [24]. The other important property of SiC is a low neutron cross section which allows chain reaction because of its resistance to radiation [25]. Therefore, this makes SiC important for high-temperature applications.

Silicon carbide consists of equal amounts of silicon (Si) atoms and carbon (C) atoms. SiC has a tetrahedral structure, with each C atom covalently bonded to four Si atoms. The tetrahedron structure can either be CSi_4 or SiC_4 [20], as shown in figure 1.2. Despite the chemical bond being mainly covalent, the electronegativity difference adds an ionic contribution to the bonding.
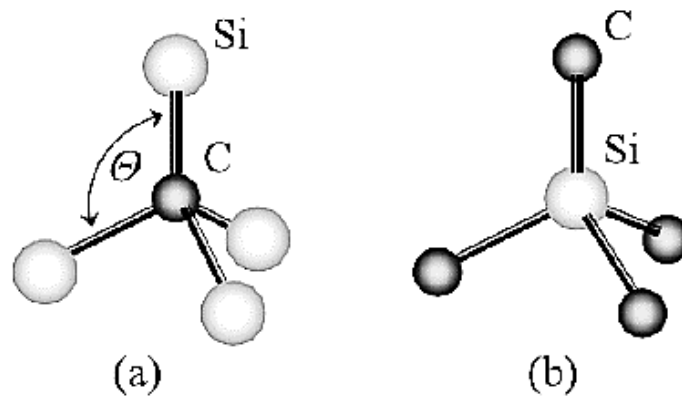
Figure 1. 2: Tetrahedral SiC structure showing (a) A carbon atom bonded to four silicon atoms (CSi_4) and (b) a silicon atom bonded to four carbon atoms (SiC_4) [5].

There are more than 200 polytypes of SiC known to exist theoretically [26]. The stacking sequence of the close-packed atomic planes determines the structure of each polytype. 3C-SiC (also known as ß-SiC), 4H-SiC, 6H-SiC, and 15R-SiC (all called α-SiC) are the most common ones and are shown in figure 1.3. Using the number, the atomic planes repetition is specified, and C, H, and R represent cubic, hexagonal and rhombohedral crystal lattices, respectively [20]. Due to the periodic stacking sequence of the wurtzite ABAB... and hexagonal symmetry, it can be doubled and tripled to form hexagonal polytypes. [27]. A hexagonal (H) arrangement occurs when a layer is surrounded on either side by different identical layers. Whereas if there are different layers on either side, it is in a cubic (c) arrangement. In this study a polycrystalline SiC composed of mainly cubic polytype was used [20].
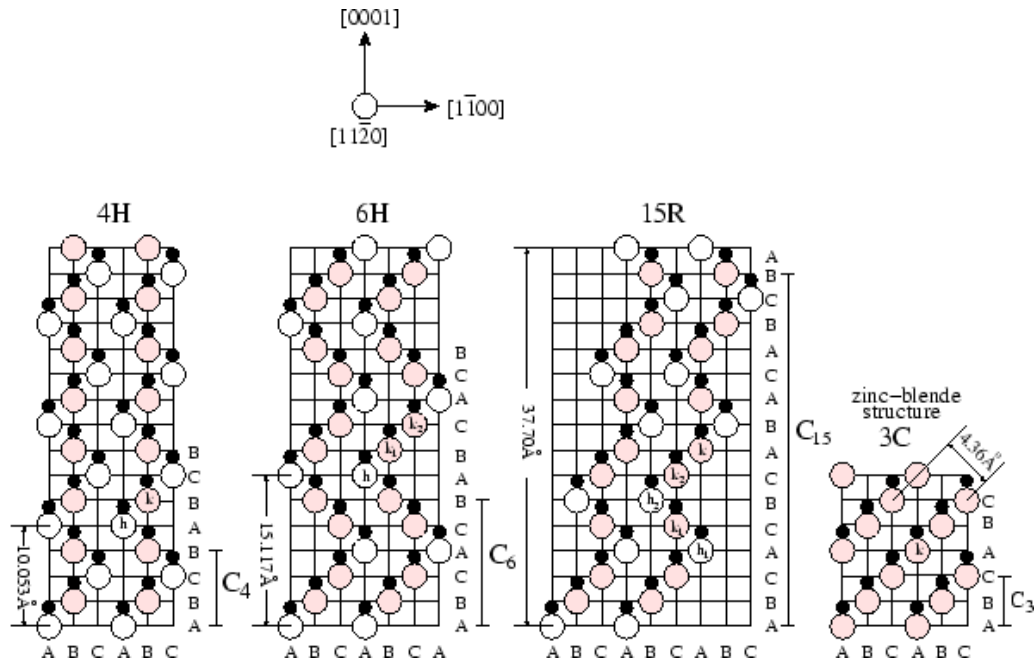
Figure 1. 3: The stacking sequence for SiC polytypes in the (1120) plane. (a) 4H-, (b) 6H-, (c) 15R- and (d) 3C-SiC [28].

A reactor's safety and failure are dependent on the integrity and the ability of the coating layers to contain all fission products [29]. Silicon carbide (SiC), as the main barrier for containment, is very effective in retaining fission products. However, some fission products like strontium (Sr), europium (Eu) and silver (^{110m}Ag) were reported to be released during operation [20]. ^{110m}Ag is a strong gamma-ray emitter with a long half-life of about 253 days [30]. ^{110m}Ag is product of a stable ^{109}Ag capturing a neutron. Although ^{109}Ag has a low fission yield (0.03% for ^{235}U), conversion rate of 0.1%, and high gamma-rays dose rate of ^{110m}Ag still pose danger.

In response to the problem with silver, for over 40 years, immense research has been done to explain how silver is transported in SiC, including out-of-pile release measurements from irradiated TRISO fuel [31, 33] and ion implantation [34, 37]. A study by Hlatshwayo *et al.* [34] investigated the diffusion after annealing of silver implanted in 6H-SiC. They performed implantations at room temperature (23 °C), 350 °C and 600 °C. Implantation at room temperature distorted the crystal structure entirely, and implantation at 350 °C and 600 °C introduced defects in 6H-SiC while the crystal structure was still intact. As the implantation temperature increased, the number of defects decreased. They found that the diffusion of silver in the room temperature implanted samples commenced after annealing at 1300 °C. Silver diffused strongly at 1400 °C, reducing the amount of silver in the substrate. This led to the conclusion that the defect density is lower in the 350 °C and 600 °C implanted samples, thus no diffusion [34]. Friedland *et al.* [35] also investigated the diffusion of silver in hexagonal

(6H-SiC) and polycrystalline SiC. They too implanted 360 keV Ag at room temperature, 350 °C and 600 °C temperatures. In their study, after 10 hours of isothermal annealing at 1300 °C, diffusion of Ag implanted at 350 °C was observed in both 6H-SiC and polycrystalline SiC. This diffusion was said to be caused by implantation induced radiation damage. Further annealing at the same temperature for 80 hours did not result in increased diffusion in the 6H-SiC samples but was increased in polycrystalline SiC. They reported that the increased diffusion in polycrystalline-SiC may be resulting from grain boundary following Fickian diffusion. Thus consequently concluded that Ag diffused through grain boundaries at temperatures above 1100 °C in polycrystalline SiC. [35].

As part of the fission process in nuclear reactors, fission products are released together with helium (He) coming from actinide radioactive decay and neutronic transformation [38]. The nuclear reactions in a nuclear reactor produce a multitude of alpha particles. In advanced fission reactors, 2.5 appm He/dpa is the generation rate reported for He [39]. It has been reported that He forms bubbles in SiC [40]. The formation of bubbles causes detrimental effects on the mechanical integrity of SiC (e.g. cracking, swelling, and exfoliation) when used in a nuclear environment [41, 42]. This integrity compromise might result in SiC losing its legitimacy as the main diffusion barrier of fission products. In contrast to silver, little to no studies have investigated the impact of helium bubbles on the migration behaviour of essential fission products. Recently, the effect of He bubbles on the migration behaviour of Ag was studied and found to promote the migration of Ag implanted into SiC at RT after annealing at 1100 °C for 5 hours [43]. The study reported that only annealed co-implanted SiC showed Ag migration towards the surface and bulk, which led to the loss of Ag from the surface. Annealing at 1100 °C also resulted in complete out-diffusion of implanted He in the polycrystalline SiC [43]. In same study Hlatshwayo *et al.* [43] suggested that more investigations are needed to understand the Ag diffusion in SiC in the environments similar to nuclear reactors. In nuclear reactors Ag co-exist with He at elevated temperature. Hence, the effect of He in the migration of Ag needs to investigated in the samples co-implanted at high temperatures.

1.1 Aim and objectives

This study aim to investigate the effect of He bubbles in SiC on the migration behaviour of silver implanted at 350 °C which is near the critical amorphization temperature of SiC of about 300 °C. This was achieved by first implanting Ag (360 keV) ions into polycrystalline SiC at 350 °C to a fluence of 2×10^{16} cm^{-2}, followed by implanting He (17 keV) ions to a fluence of 1×10^{17} cm^{-2} also at 350 °C in the same samples. The ions energies were chosen so to that they

will have the same projected range. Both Ag implanted and (Ag and He) co-implanted samples were isochronally annealed at temperatures ranging from 1000 ℃ to 1300 ℃ in steps of 100 ℃ for 5 hours, under vacuum. The as-implanted, co-implanted and annealed samples were characterized by Raman spectroscopy for microstructural changes, scanning electron microscopy (SEM) and atomic force microscopy (AFM) for topographical changes. Heavy-ion elastic recoil detection analysis (ERDA) was used to monitor the implanted species. The results were then compared to identify the role of He bubbles in the migration of the implants.

1.2 Dissertation outline

The rest of this dissertation is as follows: Chapter 2 describes the theory of diffusion. Chapter 3 deals with ion implantation. Chapter 4 discusses the analytical techniques used in this project which are Raman spectroscopy, scanning electron microscopy (SEM), Atomic force microscopy (AFM), and elastic recoil detection analysis (ERDA). The experimental procedure followed in this study is in chapter 5. Chapter 6 presents and discusses the results, and chapter 7 gives a summary of the findings and future studies.

References

1. N. Aryal, L. D. M. Ottosen, M. V. W. Kofoed, and D. Pant, 2021, Emerging Technologies and Biological Systems for Biogas Upgrading (First edition), Academic Press, London, United Kingdom.

2. F. Asdrubali, and U. Desideri. 2019, High Efficiency Plants and Building Integrated Renewable Energy Systems, Handbook of Energy Efficiency in Buildings: A Life Cycle Approach, Butterworth-Heinemann, Oxford, United Kingdom, pp. 441–595.

3. P. Moodley, and C. Trois, 2021, Lignocellulosic Biorefineries: the Path Forward, Sustainable Biofuels: Opportunities and Challenges, Academic Press, an Imprint of Elsevier, London, United Kingdom, pp. 21–42.

4. S. K. Krishnan, S. Kandasamy, and K. Subbiah, 2021, Fabrication of Microbial Fuel Cells with Nanoelectrodes for Enhanced Bioenergy Production, Nanomaterials: Application in Biofuels and Bioenergy Production Systems, Academic Press, London, United Kingdom, pp. 677–687.

5. Gareiou, Zoe, E. Drimili, and E. Zervas, 2021, Public Acceptance of Renewable Energy Sources, Low Carbon Energy Technologies in Sustainable Energy Systems, Elsevier, London, United Kingdom, pp. 309–327.

6. L. Ashok Kumar, V. Indragandhi, and Y. Uma Maheswari, 2020, PVSYST, Software Tools for the Simulation of Electrical Systems, Academic Press, pp. 349-392.

7. P. Breeze, 2019, Solar Power, Power Generation Technologies, Newnes, Oxford, United Kingdom, pp. 293–321.

8. S. P. Deolalkar, 2016, Solar Power, Designing Green Cement Plants, Butterworth-Heinemann, Oxford, United Kingdom, pp. 251-258.

9. A. R. Beig, and S. M. Muyeen. 2016, Wind Energy, Electric Renewable Energy Systems, Academic Press, Amsterdam, Netherlands, pp. 60–77.

10. N. E. Bassam, 2021, Wind Energy, Distributed Renewable Energies for off-Grid Communities: Empowering a Sustainable, Competitive, and Secure Twenty-First Century (Second edition), Elsevier, Amsterdam, Netherlands, pp. 149–163.

11. N. Belyakov, 2019, Wind Energy, Sustainable Power Generation: Current Status, Future Challenges, and Perspectives (First edition), Academic Press, London, United Kingdom, pp. 397–415.

12. N. E. Bassam, P. Maegaard, and M. L. Schlichting, 2013, Distributed Renewable Energies for Off-Grid Communities: Strategies and Technologies toward Achieving Sustainability in Energy Generation and Supply, Newnes, Oxford, United Kingdom, pp. 167-174.

13. T. Mohamed, 2021, Hydropower, Distributed renewable energies for off-grid communities: (Second Edition), Elsevier, Amsterdam, Netherlands, pp. 213-230.

14. P. Breeze, 2019, Hydropower, Power Generation Technologies (Third Edition), Newnes, Oxford, United Kingdom, pp. 173-201.

15. https://nnr.co.za/what-is-nuclear-energy. (Accessed December 2, 2021)

16. S. Şahin, and Y. Wu. 2018, Fission Energy Production, Comprehensive Energy Systems, Elsevier, Amsterdam, Netherlands, pp. 590–637.

17. B. Viswanathan, 2017, Nuclear Fission, Energy Sources: Fundamentals of Chemical Conversion Processes and Applications, Newnes, Oxford, United Kingdom, pp. 113–126.

18. P. G. Kosky, R. T. Balmer, W. Keat, and G. Wise, 2021, Nuclear Engineering, Exploring Engineering: An Introduction to Engineering and Design (Fifth edition), Academic Press, London, United Kingdom, pp. 341–360.

19. www.pbmr.co.za/index2.asp?Content=194 (Accessed December 2, 2021).

20. J. B. Malherbe, 2013, Diffusion of fission products and radiation damage in SiC, Journal of Physics D, 46, pp. 473001.

21. 0www.nuclearpoweryesplease.org/blog/2012/01/05/good-news-of-2011-in-review/pebble_disection (accessed December 2, 2021).

22. S. Sömiya, and Y. Inomata, 1991, Silicon Carbide Ceramics-1: Fundamental and Solid Reaction, Elsevier Applied Science, London, England.

23. A. J. Ruys, and I. G. Crouch, 2021, Chapter 7 - Siliconized Silicon Carbide, Metal-Reinforced Ceramics, Woodhead Publishing, Amsterdam, Netherlands, pp. 211–283.

24. R. J. Kuhudzai, J. B. Malherbe, T. T. Hlatshwayo, N. G. Van Der Berg, A. Devaraj, Z. Zhu, and M. Nandasiri, 2015, Synergistic effects of iodine and silver ions co-implanted in 6H–SiC, Journal of Nuclear Materials, 467, pp. 582-587.

25. D. A. Petti, P. A. Demkowicz, J. T. Maki, and R. R. Hobbins, 2012, TRISO-Coated Particle Fuel Performance, Comprehensive Nuclear Materials, Elsevier, Amsterdam, Netherlands, pp. 151-213.

26. T. L. Daulton, T. J. Bernatowicz, R. S. Lewis, S. Messenger, F. J. Stadermann, and S. Amari, 2003, Polytype distribution of circumstellar silicon carbide: Microstructural characterization by transmission electron microscopy, Geochimica et Cosmochimica Acta, 67 (24), pp. 4743-4767.

27.0www.wikipedia.org/wiki/Polymorphs_of_silicon_carbide#Summary_of_polytypes (Accessed January 24, 2022).

28. R. Khazaka, 2016, From atomic level investigations to membrane architecture: an in-depth study of the innovative 3C-SiC/Si/3C-SiC/Si heterostructure (Doctoral thesis, François-Rabelais University of Tours).

29. K. Sawa, 2012, TRISO Fuel Production, Comprehensive Nuclear Materials, Elsevier, Amsterdam, Netherlands, pp. 143-149.

30. P. Demkowicz, J. Hunn, R. Morris, J. Harp, P. Winston, C. Baldwin, F. Montgomery, S. Ploger, and I. V. Rooyen, 2012, Preliminary results of post-irradiation examination of the AGR-1 TRISO fuel compacts (No. INL/CON-12-24427). Idaho National Lab. (INL), Idaho Falls, ID (United States).

31. P.E. Brown, and R.L. Faircloth, 1976, Metal fission product behaviour in high temperature reactors-UO2 coated particle fuel, Journal of Nuclear Materials, 59(1), pp.29-41.

32. R. E. Bullock, 1984, Fission-product release during postirradiation annealing of several types of coated fuel particles, Journal of Nuclear Materials, 125 (3), pp. 304-319.

33. J. J. Van der Merwe, 2009, Evaluation of silver transport through SiC during the German HTR fuel program, Journal of Nuclear Materials, 395 (1-3), pp. 99-111.

34. T. T. Hlatshwayo, J. B. Malherbe, N. G. Van Der Berg, L. C. Prinsloo, A. J. Botha, E. Wendler, and W. Wesch, 2012, Annealing of silver implanted 6H–SiC and the diffusion of the silver, Nuclear Instruments and Methods in Physics Research Section B: Beam Interactions with Materials and Atoms, 274, pp. 120-125.

35. E. Friedland, J. B. Malherbe, N. G. Van der Berg, T. T. Hlatshwayo, A. J. Botha, E. Wendler, and W. Wesch, 2009, Study of silver diffusion in silicon carbide, Journal of Nuclear Materials, 389 (2), pp. 326-331.

36. T. T. Hlatshwayo, J. B. Malherbe, N. G. Van Der Berg, A. J. Botha, and P. Chakraborty, 2012, Effect of thermal annealing and neutron irradiation in 6H-SiC implanted with silver at 350 C and 600 C, Nuclear Instruments and Methods in Physics Research Section B: Beam Interactions with Materials and Atoms, 273, pp. 61-64.

37. H. J. MacLean, 2004, Silver transport in CVD silicon carbide (Doctoral thesis, Massachusetts Institute of Technology).

38. Gilbert, M. R., and Sublet, J. C. 2011, Neutron-induced transmutation effects in W and W-alloys in a fusion environment, Nuclear Fusion, 51 (4), pp. 043005.

39. H. L. Heinisch, L. R. Greenwood, W. J. Weber, and R. E. Williford, 2004, Displacement damage in silicon carbide irradiated in fission reactors, Journal of Nuclear Materials, 327 (2-3), pp. 175-181.

40. M. F. Beaufort, M. Vallet,J. Nicola, E. Oliviero, and J. F. Barbot, 2015, In-situ evolution of helium bubbles in SiC under irradiation, Journal of Applied Physics, 118 (20), pp. 205904.

41. M. F. Beaufort, F. Pailloux, A. Declémy, and J. F. Barbot, 2003, Transmission electron microscopy investigations of damage induced by high energy helium implantation in 4H–SiC, Journal of Applied Physics, 94 (11), pp. 7116-7120.

42. J. F. Barbot, M. F. Beaufort, M. Texier, and C. Tromas, 2011, Swelling and stacking fault formation in helium implanted SiC, Journal of Nuclear Materials, 413 (3), pp. 162-165.

43. T. T. Hlatshwayo, C. E. Maepa, M. Msimanga, M. Mlambo, E. G. Njoroge, V. A. Skuratov, S. V. Motloung, and J. B. Malherbe, 2021, Helium assisted migration of silver implanted into SiC, Vacuum, 183, pp. 109865.

CHAPTER 2
DIFUSSION

In a crystalline lattice, diffusion is due to thermally-activated random motion, where molecules or atoms gradually move within the material [1]. Atoms are not stationary but exhibit rapid vibrations of small amplitudes at their lattice positions. When heat is applied to a crystalline solid, and its adjacent atoms gain enough energy to break the bonds between them, they can travel from one lattice position to another [2]. Therefore, diffusion is an occurrence of transport that strongly depends on concentration gradients.

2.1 The Diffusion coefficient

Examining the rate at which an atom diffuses in a material, as indicated by the diffusion coefficient *(D)*, can acquaint us with the diffusion process. Fick's first law describes atoms' random motion as a consequence of atomic flux *(J)* and total flux is dependent on the concentration gradient [2, 3]. The mathematical formulation of Fick's first law is given by equation 2.1. In one dimension, this law is as follows:

$$J = -D\frac{dC}{dx} \qquad\qquad 2.1$$

where C is the concentration of the diffusing substance and dC/dx is the concentration gradient. The negative sign indicates that the direction of atom flow is opposite to the concentration gradient. Fick's first law relates the number of atoms crossing a unit area per unit time with the change in atom concentration per unit length at some position *x*.

For most diffusion systems, concentration gradients change over time, modifying equation 2.1 for calculating the diffusion coefficient. Fick's second law, deduced from equation 2.1, explains this outline. The second law of Fick states that the rate of compositional change equals diffusivity multiplied by the rate at which the concentration changes [3]. Taking into account equation 2.1 and the diffusion being imminent in the positive x-direction, then:

$$\frac{dC}{dt} = -\frac{dJ}{dx} \qquad\qquad 2.2$$

Despite the concentration and flux being subject to time and position changes, respectively, equation 2.2 remains valid at any given point and time [4]:

$$\frac{\partial C}{\partial t} = -\frac{\partial}{\partial x}\left(-D\frac{\partial C}{\partial x}\right) \qquad\qquad 2.3$$

Assuming D is a constant with respect to position altering, then [5]:

$$\frac{\partial C}{\partial t} = D\frac{\partial^2 C}{\partial x^2} \qquad\qquad 2.4$$

In three dimensions, we can write diffusion as follows:

$$\frac{dC}{dt} = D\nabla^2 C \qquad\qquad 2.5$$

The boundary conditions are taken into account when solving equations 2.4 and 2.5. Diffusion coefficient *(D)* regularly observes an Arrhenius equation in the range of temperatures where diffusion occurs [6]:

$$D = D_0 e^{\left(\frac{-E_a}{kT}\right)} \qquad\qquad 2.6$$

where D_0 is the pre-exponential factor and E_a is the activation energy, k is the Boltzmann constant and T is the absolute temperature in Kelvin.

2.2 Diffusion Mechanism

In this study, Ag and He were implanted into a polycrystalline SiC and then annealed at high temperatures. Thus, it is imperative to understand the defects and their relationship to diffusion when analyzing the results. The presence of defect structures in the crystals allows atoms to move more easily. Defect structure encompasses point defects such as vacancies and interstitials (Frenkel-pairs) as well as planar defects (dislocation or stacking faults), complex defects (defect resulting from clustering of point or planar defects) and grain boundaries [7]. The diffusion process occurs when an atom has enough energy to break the bonds with its neighboring atoms to occupy the empty neighbor site nearby. This section examines the main diffusion mechanisms based on the defect structure as a part of the diffusion mechanism.

2.2.1 Vacancy Mechanism

In a crystal, a vacancy is an unoccupied lattice site [6]. Diffusion of vacancies occurs when an atom jumps from its lattice position to fill a vacant position [5]. Since the atom's location remains unoccupied, the vacancy on its own seems to be moving. Figure 2.1 shows the

schematic illustration of this diffusion mechanism. In this figure, the solid circles represent the atoms and, the dotted circle represents the vacancy.
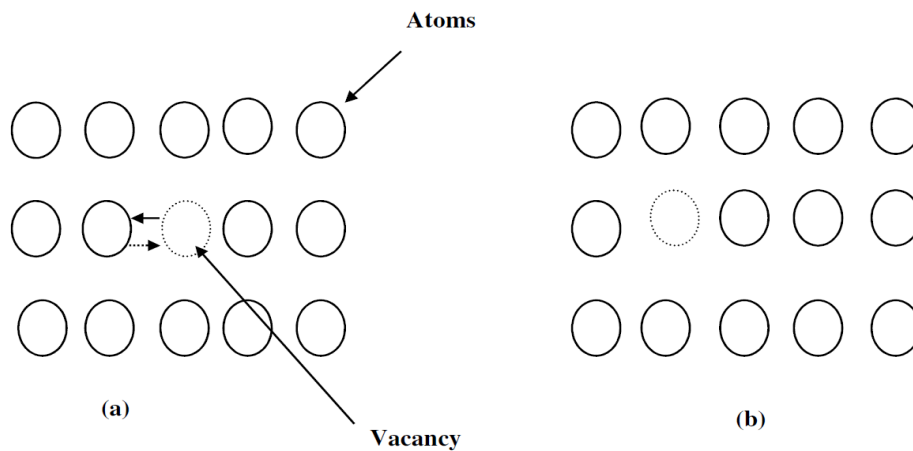
Figure 2. 1: Schematic diagram of vacancy diffusion mechanism, representing the position of the vacancy (a) before and (b) after diffusion [6].

2.2.2 Interstitial and Interstitialcy Mechanisms

Interstitial atoms are imperfections in crystalline materials that occupy sites not occupied by structural atoms. Depending on the host atom's size, an interstitial atom may be smaller than the host atom. The diffusion occurs when an interstitial atom jumps from one interstitial site to another [6]. As there are many more interstitial sites than vacancy sites, interstitial diffusion (Figure 2.2) is more likely to occur than vacancy diffusion [1]. The weaker bond of interstitials to surrounding atoms causes this phenomenon. Another diffusion mechanism connected to interstitial diffusion is interstitialcy diffusion [5]. Here interstitial atoms are similarly sized as the host atoms in this case. An interstitial atom can move into an adjacent lattice site by displacing one of its neighbour lattice atoms out of the lattice position [1, 6].
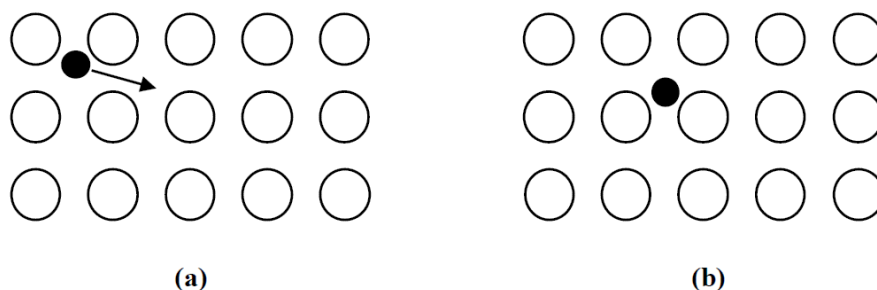
Figure 2. 2: Schematic illustration of interstitial diffusion mechanism, (a) before and (b) after interstitial diffusion [7].
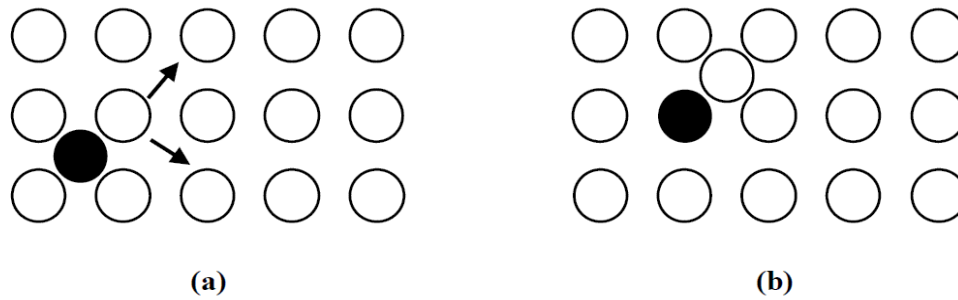
Figure 2. 3: The schematic illustration of interstitialcy diffusion mechanism, (a) before and (b) after interstitialcy diffusion [7].

2.2.3 Grain boundary Diffusion and Dislocation

Interfacial defects are defects found at the intersection of two grains with different crystallographic orientations. These defects present themselves only in polycrystalline solids and are known as grain boundaries. Essentially, they are two-dimensional alteration areas between two grains. In the intersection, there is some discrepancy between the crystal orientations of the two adjacent grains. In a grain boundary, the atoms are boundless; as a result, atoms near a grain boundary have a higher energy state than atoms in a lattice position [6]. This extra energy causes atoms to diffuse faster in the interface than in the lattice. Therefore, grain boundaries are known as high diffusivity paths [7, 8]. Dislocations are additional deficient planes in the lattice structure and are one-dimensional defects. Dislocations transpire when stress is exerted to the matrix, usually when annealed at high temperatures.

2.3 Diffusion in polycrystalline material

Materials composed of small crystalline regions with the same chemical composition, different sizes, and random crystal orientations are known as polycrystalline materials. Each crystallite region consists of a similar lattice arrangement of atoms, known as grains. Atoms in adjacent grains have a slightly different orientation, and the surface separating them is known as a grain boundary [9]. In polycrystalline materials, diffusion is a more complicated process because grain boundary diffusion is difficult to dissociate from volume diffusion since diffusing species can also escape into the lattice from the grain boundary. Thus, diffusion can occur along more than one path in polycrystalline materials. A greater level of disorder along the grain boundaries results in faster diffusion at low temperatures than within the bulk of the grains [7, 9].

References

1. D. Shaw, 1973, Atomic Diffusion in Semiconductor, Plenum Press, London, United Kingdom.

2. J. Crank, 1975, The mathematics of diffusion. Oxford University Press, Bristol, England.

3. A. Fick, 1855, On liquid diffusion, The London, Edinburgh, and Dublin Philosophical Magazine and Journal of Science, 10(63), pp.30-39.

4. R. M. Barrier, 1951, Diffusion in and through Solids, Cambridge University Press, Cambridge, England.

5. P. G. Shewmon, 1989, Diffusion in Solids (Second edition), Metals and Materials Society, Pittsburgh, Pennsylvania.

6. W. D. Callister, and D. G. Rethwisch, 2007, Materials Science and Engineering: An Introduction (Seventh edition), John Wiley, New Jersey, USA.

7. P. Heitjans, J. Karger, 2005, Diffusion in condensed matter, Springer, Amsterdam, Netherlands.

8. D. Gupta, 2004, Diffusion process in advanced technological material, Yorktown Height, New York, USA.

9. J. M. Poate, K. N. Tu and J. W. Mayer, 1978, Thin films-inter diffusion and reactions, John Wiley, New Jersey, USA.

CHAPTER 3

ION IMPLANTATION

Ion implantation is a process in which ions are accelerated and made to penetrate the surface of a solid surface. This process requires an ion source to generate ions of the desired elements, an accelerator to accelerate the ions to high energy, and a target chamber as illustrated in Fig. 3.1 [1]. The accelerated ions collide with the host/target atoms, causing the ions to gradually lose their energy and finally stopping at a certain depth below the target surface [2]. A crucial property of ion implantation is that it can precisely control the ions' penetration depth into target materials. This chapter looks at the factors which predict the ion distribution in a target material.
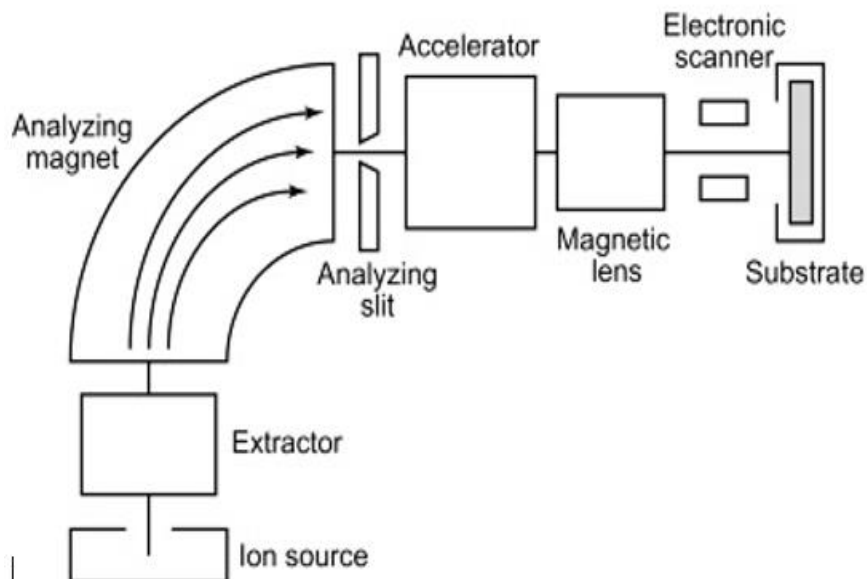
Figure 3. 1: Schematic diagram of an ion implanter [1].

3.1 Stopping power

The interactions between the projectile ions and the atoms of the target material lead to energy loss. The average decelerating force that is exerted on the projectile ion to slowing it down in the material is called the stopping power $\left(\frac{dE}{dx}\right)$ [3]. It is the quantity by which the final distribution of ions and determined, given by the following equation:

$$S = \frac{dE}{dx} \qquad\qquad 3.1$$

where E is the kinetic energy of the projectile ion and x the distance travelled by ion in the target material.

During the ion-target interaction/collision, the energetic ions lose their energy by transferring it to the host atoms. When projectile ions collide with target material, energy is transferred to the electrons (electronic stopping) or the nuclei of the material (nuclear stopping) [3]. Neither of the processes affects the other, and hence they are regarded as independent from one another. Following this, the stopping power becomes:

$$S = S_n + S_e = \left(\frac{dE}{dx}\right)_n + \left(\frac{dE}{dx}\right)_e \qquad\qquad 3.2$$

where the subscript n represents nuclear stopping and e represents electronic stopping. The contributions of the energy loss are determined by dividing the stopping power with the atomic density of the target, N. This gives the stopping cross-section, ε, as[4]:

$$\varepsilon = -\frac{1}{N} \cdot \frac{dE}{dx} \qquad\qquad 3.3$$

Thus the total stopping cross-section is:

$$\varepsilon = -\frac{1}{N}\left(\left(\frac{dE}{dx}\right)_n + \left(\frac{dE}{dx}\right)_e\right) \qquad\qquad 3.4$$
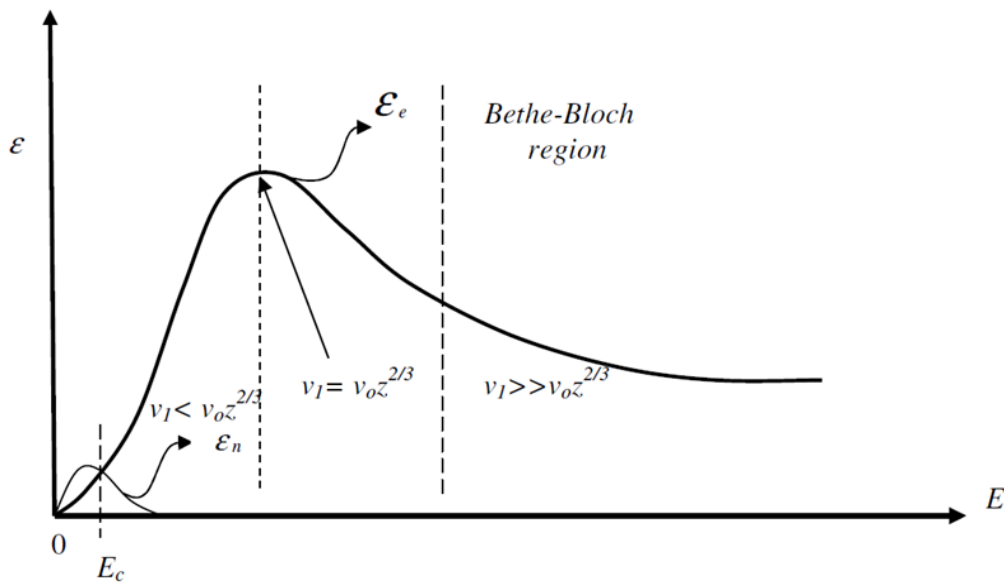
Figure 3. 2: Nuclear (ε_n) and electronic (ε_e) stopping as a function of projectile energy [5].

At low energies, nuclear stopping has more influence on the total energy loss and higher projectile masses as shown in figure 3.2. Whereas at the critical energy (E_c), the nuclear and electronic stopping are equal. Beyond the critical energy, the electronic stopping starts to have more influence and peaks before reaching the Bethe-Bloch region.

3.1.1 Nuclear stopping

Nuclear stopping is a process whereby energy is transferred through interactions between the projectile ions and the nuclei of the target atoms. The elastic Coulomb interaction results in the displacement of target atoms and the change in the projectile's direction. Isolating the ion-nucleus interaction to get a two-body elastic collision [6], figure 3.3 shows the behaviour of the nuclear scattering process.
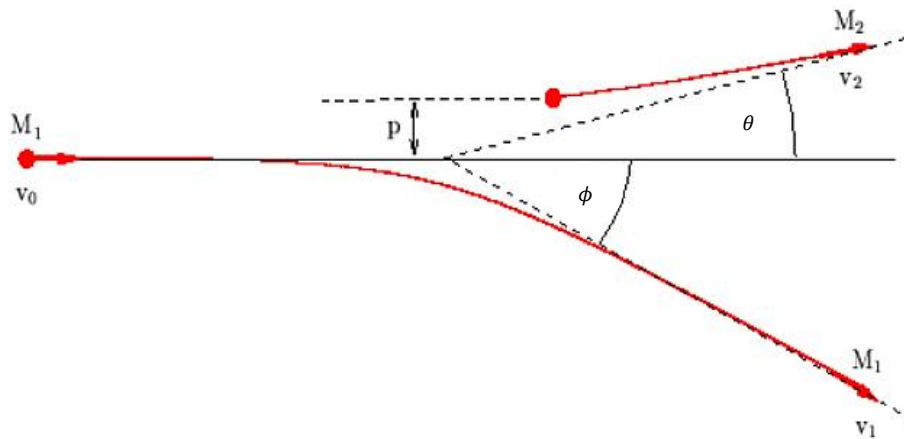
Figure 3. 3: Schematic diagram of nuclear scattering process [5].

where M_1 and M_2 are the masses of the projectile ion and target atom, respectively; v_0 is the initial velocity of projectile ion, v_1 is the final velocity of the projectile ion, and v_2 is the velocity of the target atom. P is the impact parameter, and θ and ϕ are the scattering and recoil angles, respectively.

Elastic collision suggests energy and momentum is conserved. From projectile and target masses, the scattering angle (θ) and energy of the projectile (E_0). The transferred kinetic energy, T, is given as [6]:

$$T = E_0 \cdot \frac{4M_1 M_2}{(M_1 + M_2)^2} \sin^2\left(\frac{\theta}{2}\right) \qquad 3.5$$

The interatomic potential, $V(r)$, between the two positive particles is repulsive. This causes ion scattering and hence the momentum transfer between the projectile and target atoms. The nuclear scattering can be described by multiplying the Coulomb potential by the screening function [7]:

$$V(r) = \frac{Z_1 Z_2 e^2}{4\pi\varepsilon_0 r} \phi\left(\frac{r}{a}\right)$$

$\quad$ 3.6

where Z_1 and Z_2 are the atomic numbers of the projectile ion and of the target atom, respectively; ε_0 is the permittivity of free space, r is the distance between nuclei, e is the electronic charge, and a is the screening length [7].

3.1.2 Electronic stopping

A process in which the projectile ions transfer their energy to the electrons in target atoms when impinging the material is called electronic stopping. The incident ions can transfer kinetic energy to the target electrons through multiple processes [8]. These processes include electron-electron collisions, excitation or ionization of target atoms, and excitation, ionization, or electron-capture of the incident ion [9]. There is no simple explanation for electronic energy loss due to the complexities of these processes. Hence, different models are applied to describe this process based on ion velocity. It is normal to partition the energy loss process into three parts based on the ion velocity (v_i) and the Bohr velocity ($v_o = e^2/\hbar$ where e is the electron charge and $\hbar$ is the reduced Planck's constant).

The first part of the model is apportioned to the low-energy region. In this region, the ion velocity is less than the Bohr velocity of the electrons, $v_1 < v_0 Z_1^{2/3}$. The ions cannot excite the electrons to unoccupied states because their energies are much lower than Fermi level. In this case, the ion cannot transfer enough energy to the electrons in the lower energy levels than the Fermi level to excite the electrons to unoccupied states. Therefore, only electrons in the energy level near the Fermi level are involved in energy loss. Assuming a free electron gas with a density ρ that varies with location, the electronic stopping cross-section of an ion Z_1 is given by [10]:

$$\varepsilon_o = \int I(v, \rho) \left(Z_1(v)\right)^2 \rho dV$$

$\quad$ 3.7

where I is the stopping interaction of an ion of unit charge, v is the ion velocity, ρ is the free electron gas density, and dV is a volume element of the target.

The second part of the model pertains to the intermediate energy region. In this region, the ion velocity is equal to the Bohr velocity of the electrons, $v_1 \approx v_0 Z_1^{2/3}$. The ion becomes partly ionized, and the electronic stopping reaches a maximum. Projectiles' average charge state is dependent upon their energy and targets material [11].

The third part of the model focusses on the high energy region. Here the ion velocity is far greater than the Bohr velocity of the electrons, $v_1 \gg v_0 Z_1^{2/3}$. At very high velocities, the high energetic ion loses all of its electrons. Since such energies fall under the Bethe-Botch region, the electronic stopping can be expressed as equation 3.8 [14]:

$$\varepsilon_e = \frac{4\pi Z_1^2 Z_2 e^4}{m_e v_1^2}\left[\ln\frac{2m_e v_1^2}{I} - \ln(1 - \beta^2) - \beta^2 - \frac{C}{Z_2} - \frac{\delta}{2}\right] \qquad 3.8$$

where Z_1 and Z_2 are the incident ion and target atomic numbers respectively, m_e is the electron mass, v_1 is the velocity of the projectile, and $\beta = v/c$ (c is the speed of light), and v/Z_2 is the shell correction. During very high kinetic energies, the dielectric polarization of the target causes the stopping power to decrease as a result of density correction, $\delta/2$. The average ionisation potential, I, [12] is:

$$\ln I = \sum_n f_n \ln(E_n - E_0) \qquad 3.9$$

where f_n is the corresponding oscillator strengths for target atoms, E_n are the possible energy transitions, and E_0 is the ground state. The Block's rule can be used to estimate the average excitation energy of the electrons of the target as [13]:

$$I = (10 \ eV)Z_2 \qquad 3.10$$

The work presented in this study shows attentiveness in the low and intermediate energy regions. Ion implantation energy for both silver and helium is 360 keV which falls under the low energy region. Elastic recoil detection analysis performed using Au^{7+} ions with an energy of 30 MeV is in the intermediate region.

3.2 Energy loss in compounds

The energy loss described above is that of a target material comprising of a single element. In this work, the target material used is SiC, which is a compound. Now this section will be looking at the energy loss in multiple elements.

For targets with multiple elements, collisions are still considered independent experiences that occur in succession [14]. A compound that has A and B as elements has an A_mB_n composition. Compound A_mB_n has the following total stopping cross section:

$$\varepsilon^{A_mB_n} = m\varepsilon^A + n\varepsilon^B \qquad\qquad 3.11$$

where *m* and *n* are the relative molar fractions of the compound.

Equation 3.11 is known as Bragg's rule. A slight deviation from Bragg's s rule can be observed experimentally due to the chemical and physical state of the material [15]. In cases of solid compounds, there are deviations of about 10% to 20% from Bragg's rule for the stopping maximum. This is due to the difference in atomic weight between light organic gases and solid [14]. In order to correct the chemical and physical state of the medium and the resulting energy loss, a new model is necessary. The chemical state effects were accounted for by The Core and Bonds model (CAB) was developed by Ziegler [15]. The stopping of ions in compounds in this model is assumed to be the result of two contributing factors. There are two types of effects caused by nonbonding electrons (core electrons) and valence electrons (external electrons). It is possible to determine the CAB correction of a compound by knowing its bond structure.

3.3 Energy straggling

In a material, an excited ion loses energy through many interactions with the target atoms. As a consequence, the interactions are discrete, leading to statistical fluctuations. The same energetic ions passing through a target with a thickness *(x)* will not be at the same energy after passing the same thickness on the same target. The phenomenon responsible for this is known as energy straggling [16].

Straggling has been computed from the Bloch-Bethe equation for electronic energy loss caused by statistical fluctuations in electronic interactions [16, 17]. This Bohr straggling is given by:

$$\Omega_B^2 = 4\pi Z_1^2 Z_2 e^4 Nx \qquad\qquad 3.12$$

where Ω_B^2 is the Bohr's energy straggling, Z_1 and Z_2 are the projectile and target atomic numbers, respectively, *N* is the atomic density and *x* is the thickness of the target. Therefore, the full width at half maximum (*FWHM*) of energy loss distribution is given by [10]:

$$FWHM = 2\Omega_B\sqrt{2\ln 2} \qquad\qquad 3.13$$

Lindhard *et al.* [10] extended Bohr's point charge assumption by including a correction term for energy levels where these assumptions may not apply [10]. As in Bragg's law for energy loss, the total energy straggling is calculated by a linear additively rule for compound targets.

3.4 Range of implanted ions

Range is the actual distance traveled by ion from the surface to a point where it is embedded within the target material. The average range of the ions can be determined by integrating the energy loss [18], and is given as:

$$R = \frac{1}{N} \int_0^{E_0} \frac{1}{dE/dx} dE \qquad\qquad 3.14$$

where N is the number of atoms per unit volume, E_0 is the incident energy of the projectile ion as it impinges the target material.

Energy lost in each collision, and the distance travelled between collisions are random. Therefore, not all ions of a certain type and incident energy have the same range. This leads to a great deal of scattering at the depths to which individual ions penetrate. The distribution in ranges is referred to as the range straggle. The depth of penetration of the ions is called the projected range (R_p) [19]. Figure 3.4 illustrates the projected range, R_p and the total range, R, for an incident ion on a target material.
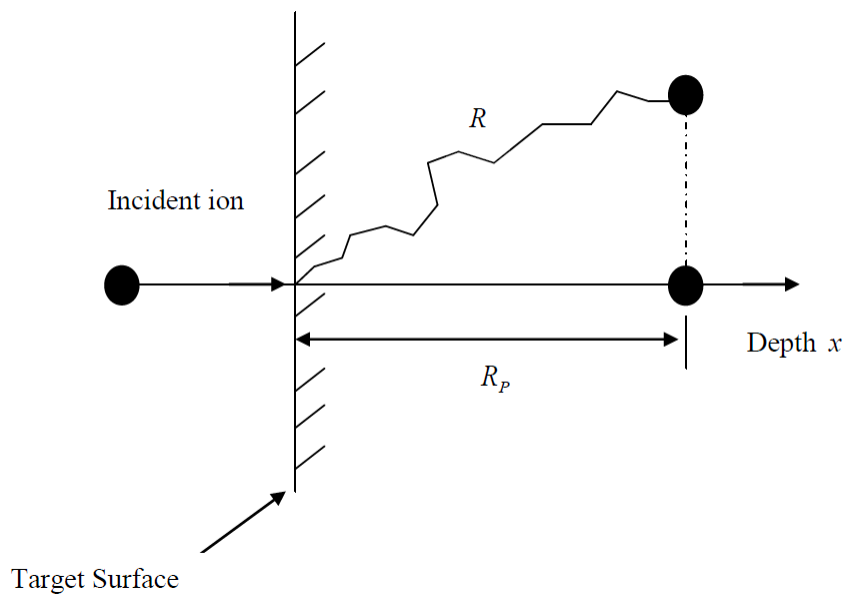
Figure 3. 4: Schematic diagram of an ion incident on a target material with total range R and projected range R_p.

3.5 Radiation damage

Radiation damage to a crystalline target occurs when an energetic ion moves into a solid target and transfers enough energy to a target atom to dislodge it from its lattice site [20]. The extent of radiation damage relies on the type of projectile ion, the material of the target, the implantation fluence, and temperature [21]. High-energy projectiles transfer part of their kinetic energy to the target atoms and displace them from their lattice positions. The energy transferred is adequate to overcome the binding energy. The liberated atoms will continue to collide with other atoms, displacing them while transferring part of their energy. This will continue until all energy is lost and moving ions/atom has come to rest. The least amount of energy necessary to displace an atom from its lattice position is called displacement energy (E_d) [22]. The substrate used in this study is silicon carbide, and the displacement energy of silicon and carbon are 35 keV and 20 keV, respectively [21].

Light ions transfer the least amount of energy due to few interactions with the target atoms [23]. As the light ion loses energy towards the end of the range, nuclear stopping becomes dominant. Heavy ions during collisions transfer large amounts of energy, displacing target atoms. The displaced atoms continue to displace other target atoms. Compared to light ions, these ions experience a reasonably higher degree of nuclear stopping [19]. Figure 3.5 shows a schematic diagram of damage distribution in the lattice structure for heavy and light ions.
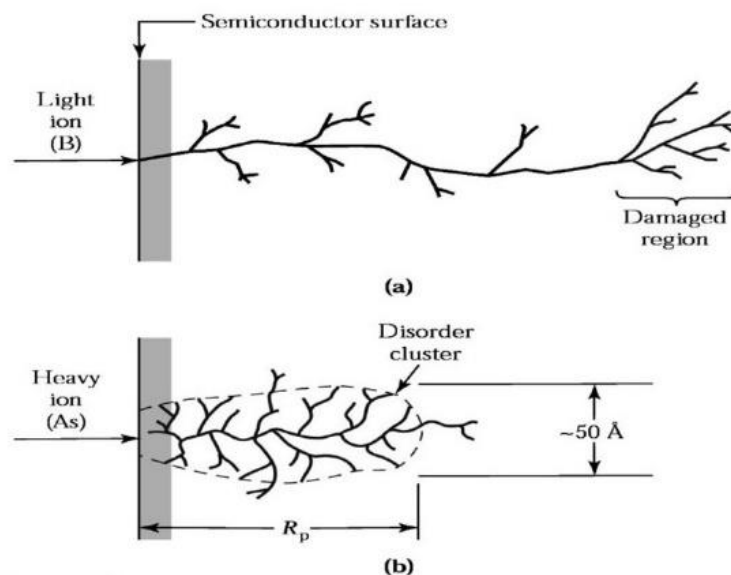
Figure 3. 5: Schematic diagram of damage distribution (a) light ion and (b) heavy ion [24].

3.6 Simulation of ion implantation (SRIM)

Ion implantation simulation is performed to predict the experimental results before implantation. In this study, Stopping and Range of Ions in Matter (SRIM) software was used to simulate the implantation of silver (Ag) and helium (He) into silicon carbide (SiC). SRIM is software used to calculate the stopping and range of ions as a result of ion-matter interactions. The SRIM software is based on Monte Carlo simulation, which creates a model of possible outcomes using a probability distribution. SRIM is used to determine ion range, damage, and distribution within an amorphous target. The program does not account for the channeling of impinging ions [25]. The SRIM program assumes the following:

- The ion-target interaction is binary, and ignores the influence of the surrounding atoms.
- The target is an amorphous material and, any changes in the crystal structure are ignored.
- The recombination of displaced atoms and vacancies is also ignored.
- The ion changes direction due to binary collisions and only the projected range is affected by these collisions.
- The thermal effects in the solid are not taken into account i.e. redistribution of the implanted ions in target due to this effects is neglected.
- The electronic stopping power of the ions is an averaging fit of data from a large number of experiments.

With all its assumptions, the program still maintains a decent level of precision with an error of about 5-10% [8].

References

1. J. X. Zhang, and K. Hoshino, 2019, Chapter 2 – Fundamentals of nano/microfabrication and scale effect in Micro and Nano Technologies, Molecular Sensors and Nanodevices (Second Edition), Academic Press, pp. 43-111.

2. I. Ahmad and W. Akram, 2017, Introductory Chapter: Introduction to Ion Implantation, IntechOpen, Rijeka, Croatia.

3. S. Minárik, and R. Riedlmajer, 2018, On the Problem of the Ion Energy Loss in Thin Absorbers, Research Papers Faculty of Materials Science and Technology Slovak University of Technology, 26 (43), pp. 17-24.

4. B. Bruckner, 2019, New aspects of electronic interactions of keV ions with matter (Doctoral thesis, Acta Universitatis Upsaliensis).

5. G. S. Was, 2007, Fundamentals of Materials Science: Metals and Alloys, Nuclear Engineering and Radiological Sciences, University of Michigan: Springer Berlin Heidelberg New York.

6. H. Gnaser, 1999, Low-Energy Ion Irradiation of Solid Surfaces, Springer, Berlin, Germany.

7. M. Backman, 2012, Effects of nuclear and electronic stopping power on ion irradiation of silicon-based compounds (Doctoral thesis, University of Helsink).

8. J. F. Ziegler, J. P. Biersack and U. Littmark, 1985, The Stopping and Range of Ions in Solids, The stopping and ranges of ions in matter, Pergamon Press, New York, USA.

9. P.D Townsend, P.J Chandler, and L. Zhang, 1994, Optical Effects of Ion Implantation, Cambridge University Press, Cambridge, United Kingdom.

10. J. Lindhard and M. Scharff, 1953, Energy loss in matter by fast particles of low charge, Det Kongelige Danske Videnskabernes Selskab Matematisk-fysiske Meddelesler, 27, pp. 1–32.

11. G. Bardos, and G. M. Gavrilenko. 1986, Electronic stopping power formula for energetic ions, Acta Physica Hungarica, 59 (3), pp. 393-399.

12. E. Kamaratos, 1984, The mean excitation energy for stopping power I, the Bragg rule, and chemical and phase effects, Application of a statistical treatment to the determination of I for chemically bound particles, Chemical Reviews, 84 (6), pp. 561-576.

13. F. Bloch, 1933, The slowing down of rapidly moving particles in their passing through solid matter, Annals of Physics (Leipzig), 16, pp. 285-320.

14. H. Bethe 1930, On the theory of the passage of rapid charged particle radiation through matter, Annalen der Physik, 5(3), pp. 325-400.

15. J. R. Tesmer, and M. Nastasi, 1995, Handbook of modern ion beam materials analysis, Materials Research Society, Pennsylvania, USA.

16. L. C. Feldman, and J. W. Mayer, 1986, Fundamentals of surface and thin film analysis, Elsevier Science Publishers, Amsterdam, Netherlands.

17. N. Bohr, 1948, The penetration of atomic particles through matter, Det Kongelige Danske Videnskabernes Selskab Matematisk-fysiske Meddelesler, 18 (8). pp. 144.

18. J. Gibbons, W. Johnson and S. Mylroie, 1975, Projected range statistics, semiconductors and related materials (Second Edition), Hutchingson and Ros, Pennsylvania, USA.

19. M. Nastasi, and J. W. Mayer, 2006, Ion Implantation and Synthesis of Materials, Springer, Berlin, Germany.

20. G. H. Kinchin, and R. S. Pease, 1955, The displacement of atoms in solids by radiation. Reports on progress in physics, 18 (1). pp. 1.

21. R. Devanathan, W. J. Weber, and F. Gao, 2001, Atomic scale simulation of defect production in irradiated 3C-SiC, Journal of Applied Physics, 90 (5), pp. 2303-2309.

22. H. Xiao, 2012, Introduction to semiconductor technology (Second edition), Society of Photo-Optical Instrumentation Engineers (SPIE) press, Bellingham, Washington, USA.

23. R. J. Kuhudzai, 2015, Diffusion and surface effects of Sic implanted with fission product elements (Doctoral thesis, University of Pretoria).

24. T. M. Mohlala, 2017, Migration behaviour of Europium implanted into sigle crystalline 6H-SiC (Masters Dissertation, University of Pretoria).

25. J.F. Ziegler, SRIM 2013, www.srim.org, USA.

CHAPTER 4

ANALYTICAL TECHNIQUES

This chapter discusses the experimental techniques employed to monitor the effects of implanted helium (He) in the migration behaviour of silver (Ag) implanted into polycrystalline silicon carbide (SiC) and the structural and morphological changes before and after annealing. The experimental techniques used are Raman spectroscopy, scanning electron microscopy (SEM), atomic force microscopy (AFM), and elastic recoil detection analysis (ERDA).

4.1 Raman spectroscopy

In this research, the Raman spectroscopy technique was used to study the structure of the virgin Sic and the structural changes in the implanted Sic samples before and after annealing. Raman spectroscopy is a technique that measures the vibrational energy modes in a sample using scattering of monochromatic light. The information from molecular vibrations can provide details about molecular and chemical structure, intrinsic stress, and crystallinity of the material [1].

4.1.1 Raman principle

In Raman spectroscopy a sample is bombarded with laser photons, and the molecules emit scattered photons. A bulk of the photons are scattered elastically, while a fraction of the photons are scattered in-elastically. The elastically scattered photons have the same energy (frequency and wavelength) as the incident photons and are called the Rayleigh scattering. In-elastically scattered photons have different energies than incident photons and are called Stokes or anti-Stokes. If the energy of the scattered photon is less than that of the incident photon (longer wavelength), it is called the Stokes Raman scattering. If the energy of the scattered photon is more than that of the incident photon, it is called anti-Stokes Raman scattering. [2]. Figure 4.1 shows the scattering processes that occur when light interacts with a molecule.
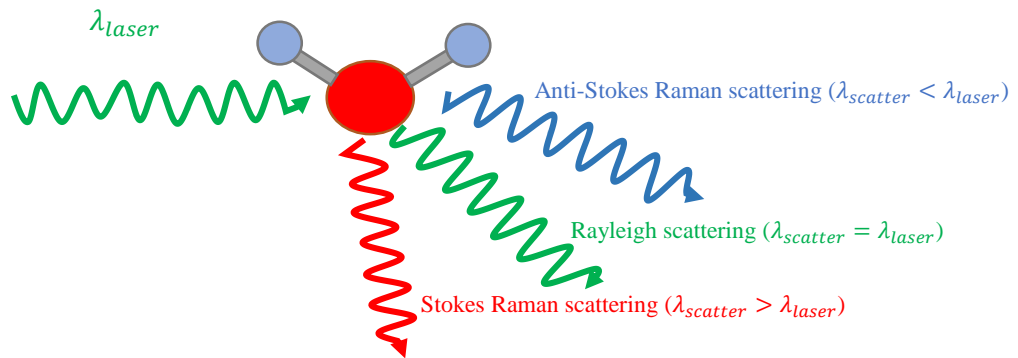
Figure 4. 1: Schematic diagram of scattering process.

When light interacts with a sample, the energy of the photon is transferred to the molecules. This gives the molecule energy to move from its original vibrational state to a virtual state. The virtual state is unstable, and photons immediately relax to a lower vibrational level emitting photons in this process. When a molecule relaxes back to its original vibrational energy state, it is called elastic scattering. When a molecule relaxes to a vibrational energy state higher or lower than its original state, it is called inelastic scattering [1]. Figure 4.2 shows quantum energy transitions for Rayleigh (elastic) and Raman (inelastic) scattering.
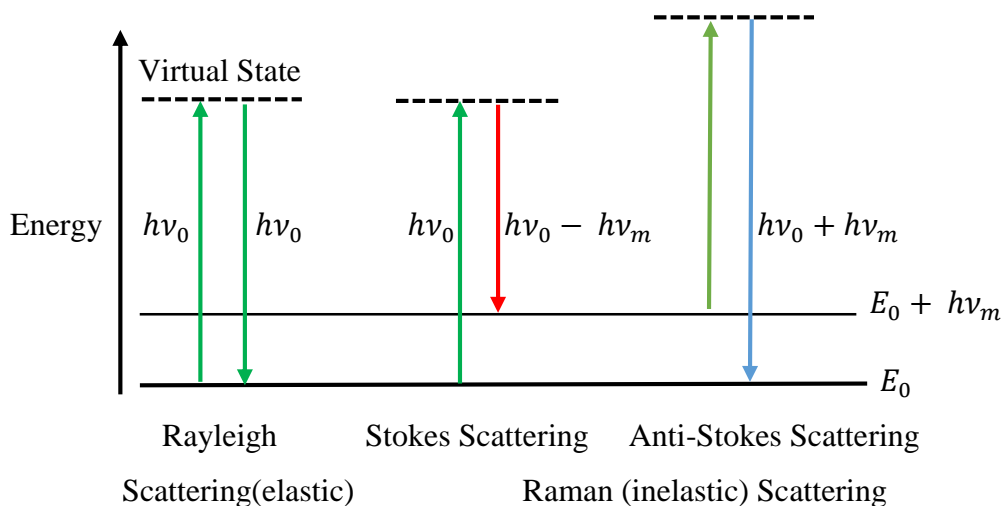
Figure 4. 2: Diagram showing energy level for Rayleigh (elastic) and Raman (inelastic) scattering.

4.1.2 Raman Effect

Raman effect is the change in vibrational, rotational, or energy of a molecule. It emerges from the interaction of an incident photon with the electric dipole of a molecule. The electric field of the incident electromagnetic wave is given as [3]:

$$\vec{E} = \vec{E_0} \cos(2\pi v_0 t) \qquad 4.1$$

where v_0 is frequency of the incident electromagnetic wave, E_0 is the amplitude and t is time. Polarization of the electron cloud is caused by the oscillating electromagnetic field of a photon. The dipole moment $\vec{P}$ induced by the electric field $\vec{E}$ is given as [3]:

$$\vec{P} = \alpha . \vec{E} \qquad 4.2$$

where α is the polarizability of the molecule. The time dependent induced dipole moment of the electromagnetic field becomes:

$$\vec{P} = \alpha \vec{E_0} \cos(2\pi v_0 t) \qquad 4.3$$

Taking vibrational diatomic molecules as a model system and assuming simple harmonic motion, the displacement dQ of the atom near its equilibrium position is due to the oscillation mode given by [3]:

$$dQ = Q_0 \cos(2\pi v_i t) \qquad 4.4$$

where Q_0 is the amplitude of vibration, and v_i is the frequency of vibration. Approximating small displacements by Taylor series expansion, the polarizability is given by equation 4.5 [4]:

$$\alpha = \alpha_0 + \frac{\partial \alpha}{\partial Q_0} Q_0 \cos(2\pi v_i t) \qquad 4.5$$

Combining equation 4.3 and equation 4.5, gives

$$\vec{P} = \alpha_0 \vec{E_0} \cos(2\pi v_0 t) + \frac{\partial \alpha}{\partial Q} Q_0 \vec{E_0} \cos(2\pi v_0 t) \cos(2\pi v_i t) \qquad 4.6$$

Applying a trigonometric identity gives:

$$\vec{P} = \alpha_0 \vec{E_0} \cos(2\pi v_0 t) + \frac{1}{2}\frac{\partial \alpha}{\partial Q} Q_0 \vec{E_0} \{\cos[2\pi(v_0 - v_i)t] + \cos[2\pi(v_0 + v_i)t]\} \qquad 4.7$$

From equation 4.7 frequency for Rayleigh scattering is expressed as v_0, and the frequency for the Raman scattering as $(v_0 \pm v_i)$ [4].

4.2 Scanning electron microscopy

The morphological changes for the single implanted samples before and after annealing were monitored using the scanning electron microscopy. The technique is a microscope that generates images of a samples' surface by scanning it with a focused beam of high-energy electrons [5].

4.2.1 Principle of SEM

Scanning electron microscopy relies on the attraction between the electrons accelerated by electromagnetic fields having the same energies and path as atoms of the sample. Electrons are generated from the electron gun with a thermionic emitter [6]. In this study, the machine employed the field emission electron gun. Negatively charged electrons travel through the electron column at high energy and high speed. High voltage accelerates the electrons, and a system of apertures and magnetic lenses condense and focus the beam. The scanning coil scans the focused beam on the surface of the sample to create an image. The electron beam must be kept under a vacuum to prevent scattering due to collisions with other molecules [7]. Figure 4.3 shows a schematic diagram of Field Emission Scanning Electron Microscope (FESEM) technique.
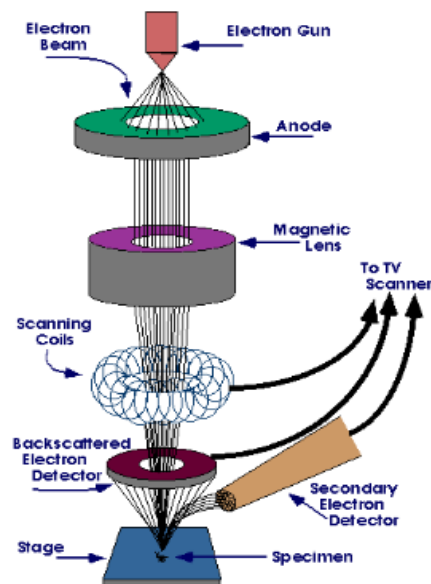
Figure 4. 3: Schematic diagram of Field Emission Scanning Electron Microscope (FESEM) [7].

4.2.2 Electron interaction with matter

When electrons interact with the sample, various signals are generated. These signals give information about the sample's surface topography, morphology, composition, and crystallography. The signal emitted includes the secondary electrons, backscattered electrons, characteristic X-rays, and Auger electrons [5]. Figure 4.4 shows the signals emitted during electron beam interaction with the sample.

Primary electron beam

Backscattered electrons   Auger electrons

Characteristic X-rays   Secondary electrons

Sample

Direct transmission beam
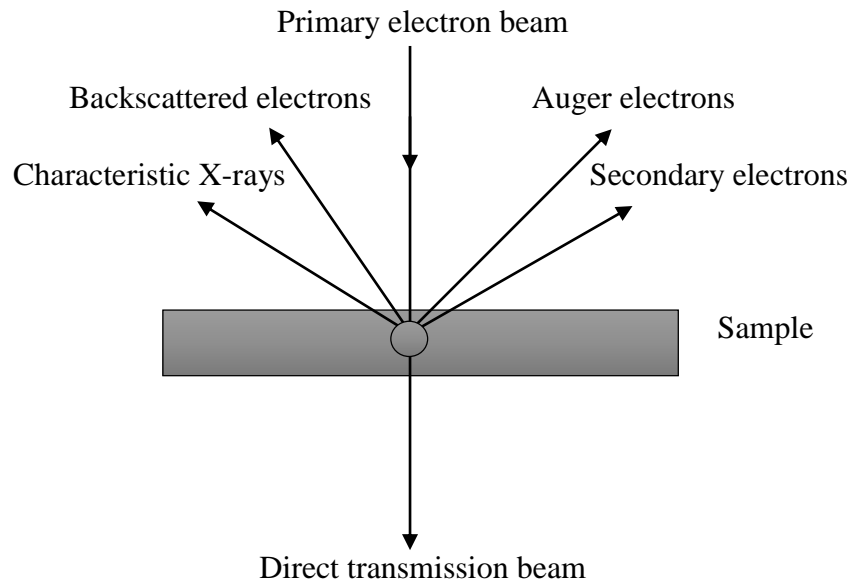
Figure 4. 4: Schematic diagram showing signals that are detected by a scanning electron microscope (SEM).

When the primary electrons come into contact with the sample, the beam of electrons will either interact with the atoms' nucleus or the electrons of the host material. The interaction between the atoms' nucleus and the primary electrons is elastic, while the interaction between the primary electrons and the host electrons is inelastic [8]. The nucleus in the host material reflects the high-energy electrons without slowing down, producing backscattered electrons. The generation of backscattered electrons depends on the weight of the element. Heavier elements with larger nuclei will backscatter more electrons and thus will appear brighter in SEM images. The difference, in contrast, is used to investigate the different chemical compositions present in a sample [8, 9].

When the high-energy electron beam transfers part of its energy to the host electrons, secondary electrons are generated. When an electron leaves the atom, it leaves a vacancy at a lower energy

level. An electron from a higher energy level falls to fill the vacancy. Excess energy is released in the form of X-rays or outer electrons. The electrons released as a result of de-energization are called Auger electrons [10]. Secondary electrons can be used to investigate the morphology of the sample. Auger electrons and X-rays have energy unique to their source element. They both are used to provide information about the chemical composition of the sample's surface [10, 11].

4.3 Atomic force microscopy

Atomic force microscopy (AFM) is an imaging technique that scans the surface of a sample. The technique uses a cantilever that is attached with a very sharp tip to scan over the sample surface. The tip is located at the end of a flexible cantilever and serves as a surface probe. A piezoelectric scanner is responsible for the lateral and vertical movement of the cantilever. A laser beam is reflected on top of a cantilever by use of highly reflective material. When the cantilever moves, the laser beam is reflected into a position-sensitive photo detector. The photo detector records the changes in direction caused by the bending of the cantilever [4]. AFM gives a precise measurement of topographical and physical properties of the samples' surface [12]. Figure 4.5 shows the schematic diagram of the AFM.
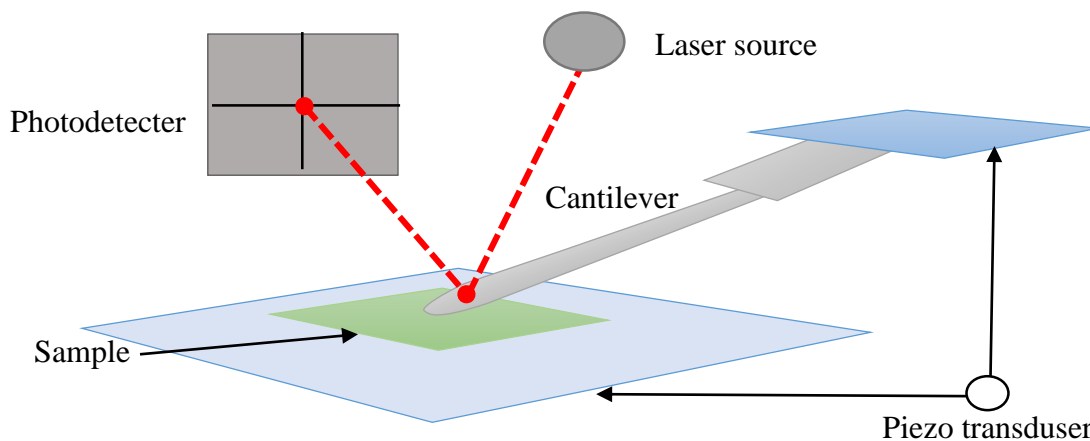
Figure 4. 5: Schematic diagram of an Atomic Force Microscope.

4.3.1 AFM principle

Atomic Force Microscopy counts on the interaction of the forces between the atoms of the tip and atoms of the sample. AFM measures the attractive and repulsive force between the atoms on the tip and the sample surface [13]. Contact and dynamic modes are used to measure the

interactions. In contact mode, the probe keeps continuous contact with the sample [11]. Due to the overlap of electron clouds of tip and sample, the force between the probe and sample is repulsive [11, 13]. Figure 4.6 shows tip-sample interaction of contact mode in AFM.
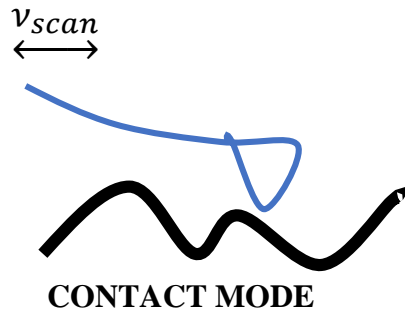
Figure 4. 6: Schematic diagram of contact mode.

The dynamic mode has two sub-modes that is tapping (intermittent contact) mode and the non-contact mode. In tapping mode, the cantilever vibrates at or near its resonance frequency. The vibration causes the probe to strike the surface for a short period due to the decrease in tip-surface distance. The decreased distance favours the repulsive force as its magnitude increases [11]. Figure 4.7 illustrates the tip-sample interaction in tapping mode.
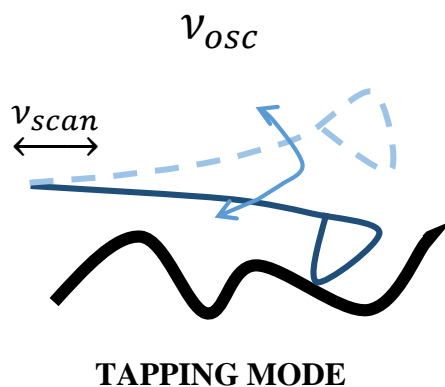
Figure 4. 7: Schematic diagram of tapping mode.

In non-contact mode, a cantilever vibrates at its resonance frequency. A smaller amplitude is kept, therefore preventing the probe from touching the sample [11]. Non-contact mode utilizes the attractive force because of dipole-dipole interactions between the atoms of tip and sample [13]. Figure 4.8 demonstrates the tip-sample interaction in non-contact mode.

$$\nu_{osc}$$

$$\nu_{scan}$$
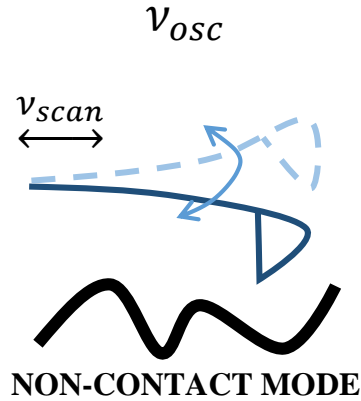
NON-CONTACT MODE

Figure 4. 8: Schematic diagram of non-contact mode.

4.4 Elastic Recoil Detection Analysis (ERDA)

The elemental depth profiles and concentration of elements in as-implanted and annealed samples were obtained using Heavy-ion elastic recoil detection analysis (ERDA) technique. The technique is an ion beam analysis (IBA) technique in material science that detects elemental concentrations and compositions of thin layer materials via elastic recoil detection [14].

The ERDA technique involves the acceleration of an ion beam toward a solid target and elastic scattering of incident ions by the target's atoms. The energy transferred from the elastic collision can be large enough such that the target nucleus recoils from the target surface [15]. The technique utilizes target atoms that have recoiled after interacting with high-energy heavy incident ions [14]. To identify the recoiled sample atoms and scattered incident ions, the ERDA has a mass-sensitive detector. It is possible to distinguish a scattered incident ion from a recoiled target atom based on the difference in energy loss in a given thickness of well-known material [16]. Light atoms recoil with more energy than the elastically scattered ions and are, therefore, easier to detect [14]. Using detection geometry, one can determine the energy loss and physical parameters of elastic scattering.

Transmission geometry is the detection of incident ions and recoils emerging at the back surface of the target. To prevent acute irreversible damage if the target breaks, the detector is be placed as close as possible to the $0°$ direction, but not directly in the direction of the incident beam. Ideally, the detector should be placed close to $0°$ direction, but not directly in the path of the incident beam to avoid significant irreversible damage in the instance of target breaking.

35

There is no need to place an absorber foil in front of a surface barrier detector since the target itself slows down the scattered ions down as they are travelling along their path [16]. Figure 4.9 clearly illustrates the geometry of transmission ERDA. The reflection geometry involves an impinging ion beam onto the target at grazing incidence and detection of recoils that emerge from the surface [15]. In front of the surface barrier detector is an absorber foil that stops ions scattered in the direction of φ as shown in Figure 4.10.
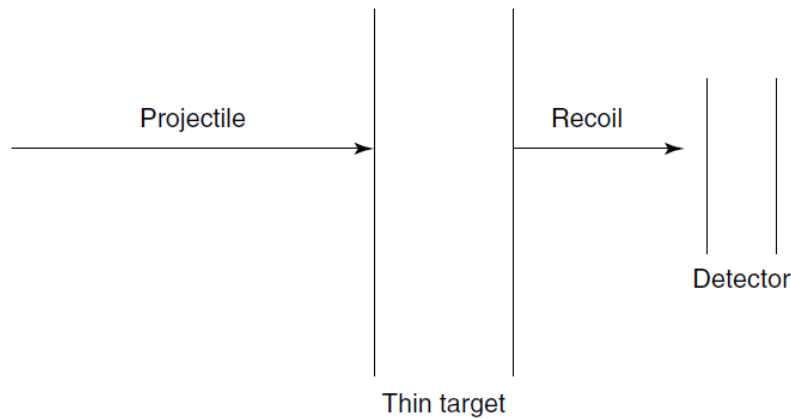
Figure 4. 7: Schematic diagram of transmission geometry [16].
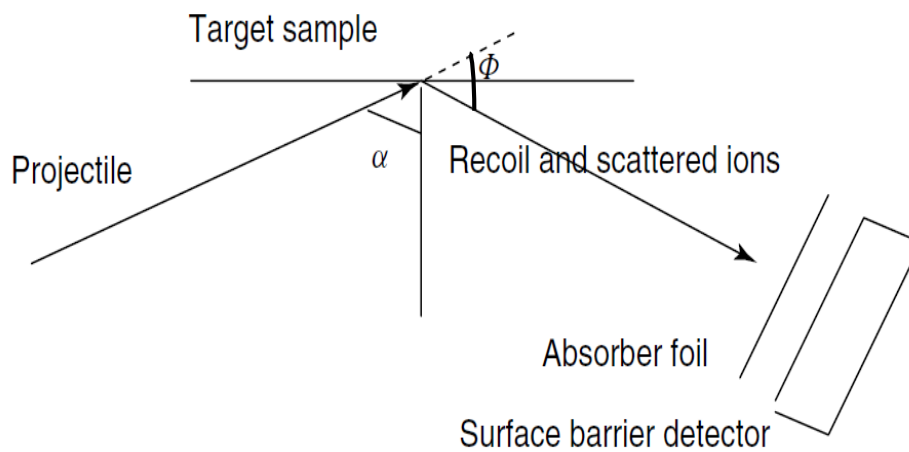
Figure 4. 8: Schematic diagram of reflection geometry [16].

When performing recoil analysis, the aim is to detect recoiling nuclei amongst the high concentration of elastically scattered beam particles. It is then necessary to place a separate absorber (from the target material) in front of the detector to exclude elastic particles. The disadvantage of this method is that the energy straggle in the absorber reduces the depth resolution [17]. A time-of-flight ERDA system has been used in this study to analyze the

samples for better resolution [15]. The atoms are recoiled from the target by using heavy ions with energies of MeV range. Time of flight (TOF) measures the energy and flight time of randomly recoiled atoms to separate all elements according to energy and mass [16]. The spectrometry measures the particle's flight time between two gates to produce two distinct signal. Figure 4.11 schematically shows a TOF spectrometer.
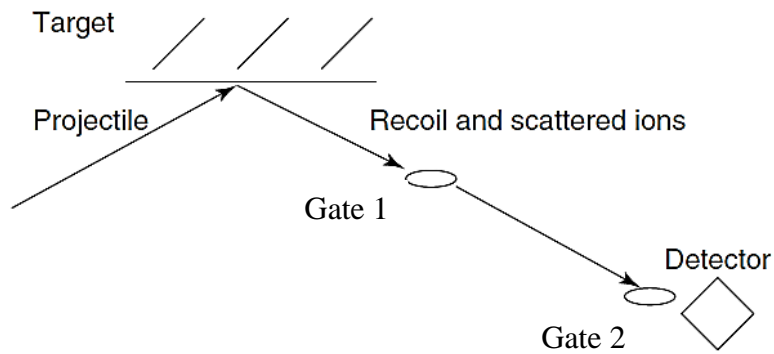
Figure 4. 9: Schematic diagram of a time of flight (ToF) spectrometer.

The mass dispersion spectrometer uses two-time detectors for consistent measurements. It consisted of two spaced carbon film micro-channel plate (MCP) time detectors and a semiconductor energy detector located at the end of the flight path. The coincidence of the flight time and recoil energy leads to the elemental separation of the recoil atoms by mass. Mass curves are developed by relating energy to the time of flight coordinates (t, E) as described by:

$$M = c(E - E_0)(t - t_0)^2 \qquad 4.8$$

where M is the mass of the recoil, t and E are time and energy coordinates in the ToF vs Energy two-dimensional scatter plots and E_0 and t_0 are calibration constants. A linear energy axis can then be created by rebinding the ToF events [18]. Elemental depth profiles can be calculated directly from linear energy spectra using the transformation algorithm, KONZERD [17]. KONZERD is used to iterate over information about the number of events in individual depth segments. This corresponds to the energy band. Two independent equations determine the relative atomic concentration n_i of element i. First is the number of counts Y_i scattered by the depth interval Δx, as shown in [19]:

$$Y_i = n_i \left(\frac{d\sigma}{d\Omega}\right) N_p \Delta\Omega \frac{\Delta x}{\sin \alpha} \qquad 4.9$$

where $(d\sigma/d\Omega)_i$ is the differential scattering cross-section, N_p is the primary beam dose, α is the angle of incidence and $\Delta\Omega$ is the detector solid angle. The energy interval ΔE_i in which i particles are scattered from depth interval Δx is given by:

$$\Delta E_i = \Delta x S_i(x) \qquad\qquad 4.10$$

where $S_i(x)$ is the energy loss factor for a depth x including contributions from the stopping of projectile and recoil. As a result of the linear additivity resulting from Bragg's rule [19], this energy loss factor is as follows:

$$S_i(x) = \sum_{j=1}^{m} n_j \left[K_i \frac{\left(dE_p/dx\right)^j}{\sin\alpha} + \frac{\left(dE_i/dx\right)^j}{\sin\beta} \right] = \sum_{j=1}^{m}\left(n_j a_{ij}\right) \qquad\qquad 4.11$$

where m is the number of elements in the target, $\left(dE_p/dx\right)^j$ and $(dE_i/dx)^j$ are stopping powers of the projectile and recoil in element j respectively, K is the kinematic factor of the recoil. A system of linear equations for each slice of thickness is found diving equation 4.9 by 4.10 resulting in:

$$\frac{Y_i}{\Delta E_i} = \frac{n_i}{\sum_{j=1}^{m} n_j a_{ij}} c_i \qquad\qquad 4.12$$

where c_i is a constant composed of the cross sections, the beam current and the detector acceptance angle [19].

References

1. K. Nakamoto, 1997, Infrared and Raman Spectra of Inorganic and Coordination Compounds (Fifth Edition), John Wiley and Sons, New York, USA.

2. U. P Agarwal, and R. H Attalla, 1995, Raman spectroscopy, Surface analysis of paper, CRC Press, Wisconsin, USA, pp.152-181.

3. D. Olego, and M. Cardona. 1982, Pressure dependence of Raman phonons of Ge and 3 C-SiC, Physical Review B, 25 (2), pp.1151.

4. O. Hollricher, T. Dieng and, J. Toporski, 2011, Confocal Raman Spectrometry, Spring Series in Optical Science, Springer, Heidelberg, Germany.

5. J. I. Goldstein, D. E. Newbury, J. R. Michael, N. W. Ritchie, J. H. J. Scott, and D. C. Joy, (2017), Scanning electron microscopy and X-ray microanalysis, Springer, New York, USA.

6. G. R. Chalmers, R. M. Bustin, and I. M. Power. 2012, Characterization of gas shale pore systems by porosimetry, pycnometry, surface area, and field emission scanning electron microscopy/transmission electron microscopy image analyses: Examples from the Barnett, Woodford, Haynesville, Marcellus, and Doig units, AAPG bulletin, 96 (6), pp.1099-1119.

7. A. H. M. Areef Billah, 2016, Investigation of multiferroic and photocatalytic properties of Li doped BiFeO3 nanoparticles prepared by ultrasonication (Dissertation, Bangladesh University of Engineering and Technology).

8. W. Zhou, R. Apkarian, Z. L. Wang, and D. Joy, 2006, Fundamentals of scanning electron microscopy (SEM), Scanning microscopy for nanotechnology, Springer, New York, USA, pp. 1-40.

9. S. K. Chapman, 1986, Working with a scanning electron microscope, Lodgemark Press, London, United Kingdom.

10. C. Scheu, and W. D. Kaplan, 2012, Introduction to Scanning Electron Microscopy, John Wiley and Sons, Weinheim, Germany.

11. S. Zhang, L. Li, and A. Kumar, 2008, Materials characterization techniques (First Edition), CRC Press, Boca Raton Florida, USA.

12. E. Meyer, 1992, Atomic force microscopy, Progress in surface science, 41(1), pp.3-49.

13. R. Bowen, and N. Hilal, 2009, Atomic force microscopy in process engineering: An introduction to AFM for improved processes and products, Butterworth-Heinemann, Oxford, United Kingdom.

14. D. D. Cohen, R. Bird, N. Dytlewski, and R. Siegele, 2003, Ion Beams for Material Analysis. Encyclopedia of Physical Science and Technology (Third Edition), Academic Press, San Diego, USA, pp. 55-63.

15. J. Tirira, Y. Serruys, and P. Trocellier, 1996, Forward recoil spectrometry: applications to hydrogen determination in solids, Plenum Press, New York, USA.

16. P. Trocellier, and T. Sajavaara, 2006, Elastic recoil detection analysis. Encyclopedia of Analytical Chemistry: Applications, Theory and Instrumentation, John Wiley and Sons Ltd, Chichester, United Kingdom.

17. G. G. Ross, B. Terreault, G. Gobeil, G. Abel, C. Boucher, and G. Veilleux, 1984, Inexpensive, quantitative hydrogen depth-profiling for surface probes, Journal of Nuclear Materials, 128, pp. 730-733.

18. M. Msimanga, D. Wamwangi, C. M. Comrie, C. A. Pineda-Vargas, M. Nkosi, and T. T. Hlatshwayo, 2013, The new Heavy Ion ERDA set up at iThemba LABS Gauteng: Multilayer thin film depth profiling using direct calculation and Monte Carlo simulation codes, Nuclear Instruments and Methods in Physics Research Section B: Beam Interactions with Materials and Atoms, 296, pp. 54-60.

19. A. Bergmaier, G. Dollinger, C. M. Frey, and T. Faestermann, 1995, Quantitative elastic recoil detection (ERD), Fresenius' journal of analytical chemistry, 353(5), pp. 582-584.

CHAPTER 5

EXPERIMENTAL PROCEDURE

This chapter outlines the experimental procedure used in this study. The morphological and structural changes caused by the co-implantation of silver and helium into silicon carbide and subsequent annealing were investigated using scanning electron microscopy (SEM), atomic force microscopy (AFM), and Raman Spectroscopy. Compositional analysis and depth profiling of as-implanted and annealed samples was performed using Heavy-ion elastic recoil detection analysis (ERDA).

5.1 Sample preparation

The polycrystalline SiC wafers from Valley Design Corporation were used as a starting substrate in this study. The as-received wafers were then washed in an ultrasonic bath with acetone, rinsed with de-ionized water, blow-dried with nitrogen gas, and finally sent for implantation. After implantation, the samples were cut and also cleaned again. The purpose of the cleaning procedure was to remove contaminants produced during cutting that could adversely affect the experiment. Figure 5.1 shows the schematic diagram of sample preparation and analysis process.

5.2 Implantation

The cleaned SiC wafers were sent for Ag implantation at Institut für Feskörperphysik, Friedrich-Schiller-Universität, Jena, Germany. The polycrystalline SiC substrate was implanted with Ag ions at the energy of 360 keV to a fluence of 2×10^{16} cm^{-2} at 350 ℃. The beam-induced target heating and channeling were minimized by keeping flux below 10^{-13} cm^{-2}s^{-1} and tilting the sample by an angle of 7° relative to the normal incidence. Some of the Ag pre-implanted samples were also implanted with He ions of 17 keV energy to a fluence of 1×10^{17} cm^{-2} and at a temperature of 350 ℃. The He implantation were performed at iThemba LABS, Gauteng, South Africa.

```
            ┌─────────────────────┐
            │  Sample preparation │
            │ (Cutting and cleaning) │
            └─────────────────────┘
                      │
                      ▼
┌──────────────────┐    ┌──────────────────┐
│  Implantation    │───▶│  Implantation    │
│  (Ag, 350 ºC)    │    │  (He, 350 ºC)    │
└──────────────────┘    └──────────────────┘
        │                       │
        ▼                       ▼
┌───────────────────────────────────────────┐
│ Annealing (at 1000 ºC,1100 ºC, 1200 ºC,    │
│              1300 ºC)                       │
└───────────────────────────────────────────┘
                      │
                      ▼
┌───────────────────────────────────────────┐
│                 Analysis                    │
│    (Raman, SEM, ERDA, and AFM)              │
└───────────────────────────────────────────┘
```
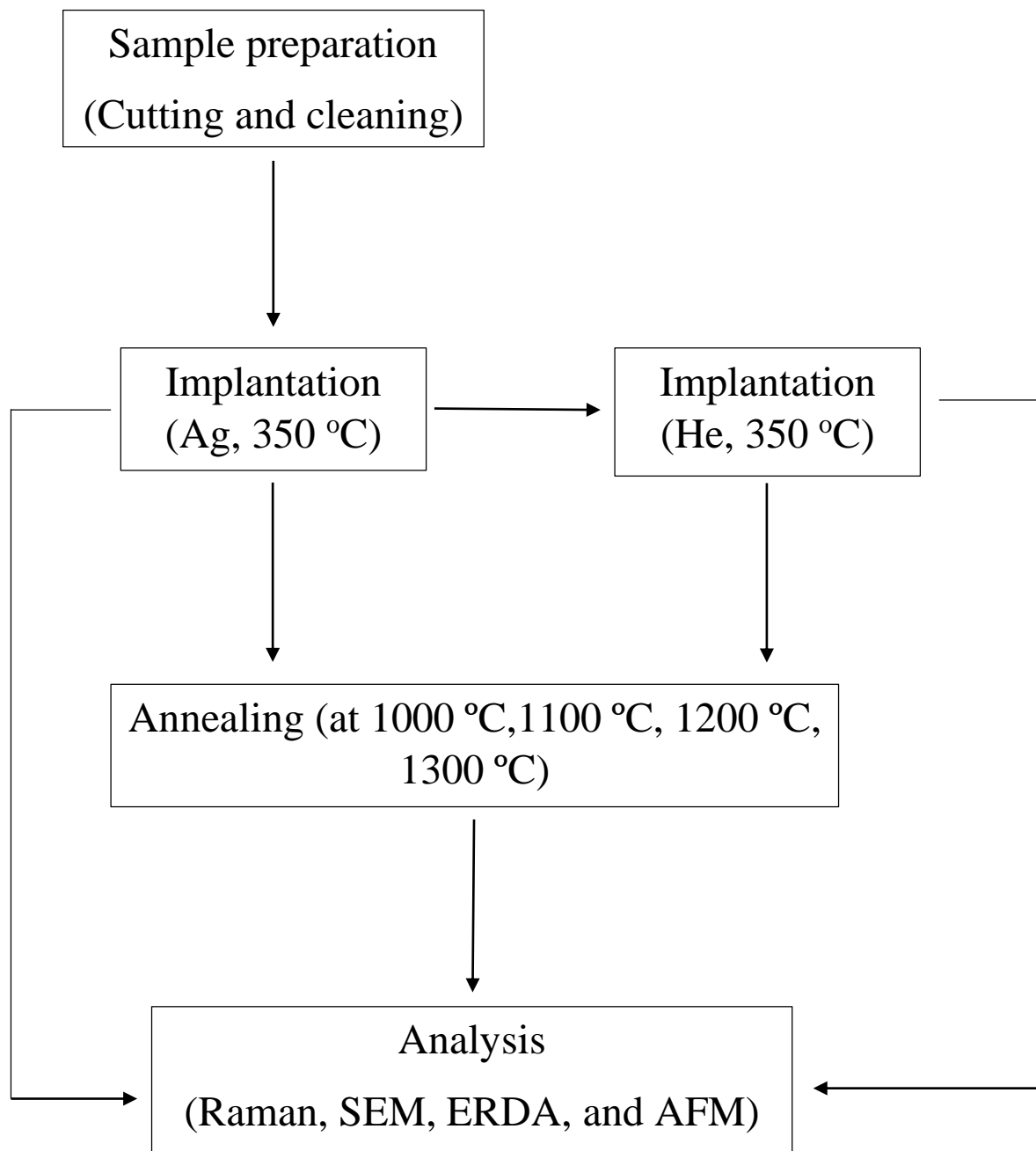
Figure 5. 1: A schematic diagram of sample preparation and analysis techniques.

5.3 Annealing of samples

After implantation, a diamond scriber was used to cut the wafer in smaller samples before annealing. The annealing was done using a computer-controlled Webb 77 graphite furnace. Both the Ag implanted and the co-implanted samples were isochronally annealed at

temperatures from 1000 ºC to 1300 ºC in steps of 100 ºC for 5 hours under vacuum. To avoid contamination in the furnace, the samples were placed in a glassy carbon crucible.

Before each annealing, the furnace was evacuated to a pressure of 10^{-6} mbar. This was followed by a degassing process, in which the furnace was heated to 200 ºC for one hour to help desorb water vapour and other gases absorbed in the internal high-temperature fibrous carbon insulation material. This also ensured that the maximum pressure during annealing was maintained at 10^{-5} mbar and reduced pumping time. A Eurotherm 2704 controller connected to a thermocouple and pyrometer was used to control the temperature. The thermocouple is used to measure temperatures below 1475 ºC, and pyrometer is used to measure temperatures above 1525 ºC [1]. The vacuum pressure increased from 10^{-6} mbar to 10^{-5} mbar, during annealing and the heating rate was kept at about 20 ºC/min. The heating element maintained each annealing temperature for a duration of 5 hours. At the end of each annealing cycle, the current was switched off to cool down the system.

5.4 Measurement conditions

5.4.1 SEM measurement

A Field Emission Scanning Electron Microscope (FEGSEM) Zeiss Ultra 55 instrument equipped with an in-lens detector was used to study the surface morphology of the Ag implanted samples before and after annealing. A voltage of 2 kV was used. Figure 5.2 shows the High-resolution Zeiss Ultra, Plus 55 instrument.

Figure 5. 2: High-resolution Zeiss Ultra, Plus 55 Scanning Electron Microscope.

5.4.2 AFM measurement

The surface morphology of the co-implanted samples were characterised using the atomic force microscopy (AFM) at the University of Pretoria. The co-implanted samples were mounted on an aluminium stub using a double sided carbon tape to ensure immobility. The AFM micrographs were generated using the Veeco Dimension Icon system with scan assist tapping mode, as shown in figure 5.3. A diamond coated tip (DDESP-FM-V2) was used, and the samples were measured at 20 μm scan size. AFM micrographs were analysed using the Nano Scope Analysis software.
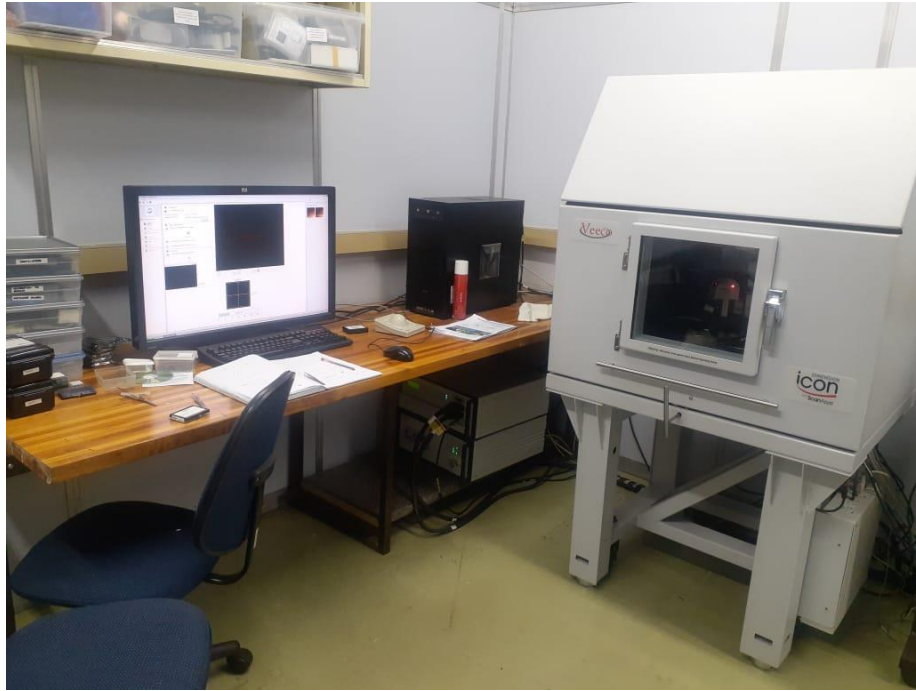
Figure 5. 3: Veeco Dimension Icon Atomic Force Microscope.

5.4.3 Raman measurement

The WITec confocal Raman microscope was used to analyse the microstructural changes of the single and dual implanted samples. The WITec alpha300 RAS+ was focused using a 100× objective lens, at an operating wavelength of 532 nm, 20mW laser power, and spectral acquisition time of 10s.

5.4.4 Elastic recoil detection analysis

Heavy-ion elastic recoil detection analysis (ERDA) was used at iThemba LABS Gauteng to monitor the implanted species in the as-implanted and annealed samples. ERDA technology detects recoil ions knocked off from the surface area of the target sample by a projectile beam that collides with the sample surface at a grazing angle of incidence of 30°. ERDA uses a Time of Flight (ToF) detector system to separate and analyse the contribution of each ion using a 30 MeV Au^{7+} ion beam. A Time of flight-energy (ToF-E) detector system consists of two carbon foil-based timing detectors, 0.60 m apart, and a silicon PIPS detector for measuring the ToF-E of the recoil ions [2]. A coincidence measurement can separate recoil particles by their atomic mass. From the 2D ToF vs Energy plots, the elemental energy spectra can be extracted and used to calculate depth profiles using the energy-depth conversion algorithm [3].

Reference

1. R. J. Kuhudzai, 2015, Diffusion and surface effects of SiC implanted with fission product elements (Doctoral thesis, University of Pretoria).

2. M. Msimanga, D. Wamwangi, C. M. Comrie, C. A. Pineda-Vargas, M. Nkosi, and T. T. Hlatshwayo, 2013, The new Heavy Ion ERDA set up at iThemba LABS Gauteng: Multilayer thin film depth profiling using direct calculation and Monte Carlo simulation codes, Nuclear Instruments and Methods in Physics Research Section B: Beam Interactions with Materials and Atoms, 296, pp. 54-60.

3. A. Bergmaier, G. Dollinger, C. M. Frey, and T. Faestermann, 1995, Quantitative elastic recoil detection (ERD), Fresenius' Journal of Analytical Chemistry, 353(5), pp. 582-584.

CHAPTER 6

RESULTS AND DISCUSSION

The effect of helium (He) and silver (Ag) ions co-implanted into polycrystalline silicon carbide at 350 °C on the structural evolution and migration behaviour of silver was investigated. Ag ions of 360 keV were implanted into polycrystalline SiC to a fluence of 2×10^{16} cm^{-2} at 350 °C. Some of the Ag implanted samples were then implanted with He ions of 17 keV to a fluence of 1×10^{17} cm^{-2} also at 350 °C. Both Ag and co-implanted samples were then annealed at temperatures ranging from 1000 °C to 1300 °C in steps of 100 °C for 5 hours. The structural changes were characterized using Raman spectroscopy while morphological and topological evolutions were characterized by scanning electron microscopy (SEM) and atomic force microscopy (AFM). The elemental depth profiles and concentration of the implants in as-implanted and annealed samples were monitored by heavy-ion elastic detection analysis (ERDA). This chapter presents and discusses the findings.

6.1 Simulation results

SRIM 2013 was used to simulate Ag ions of 360 keV and He ions of 17 keV implanted into SiC. The minimum displacement energies of 20 eV and 35 eV for carbon and silicon together with a SiC density of 3.21 g.cm^{-3} were used in the simulation [1]. The ion fluence was converted into displacement per atom (dpa) using equation 6.1 [2].

$$dpa = \frac{(^{Vac}/_{ion(Å)} \times 10^8 \times \varphi(ion.cm^{-2}))}{\rho_{SiC}(ions.cm^{-3})}$$

6.1

where, ρ_{SiC} is the atomic density of silicon carbide ($9.6419 \times 10^{22}\ atm.cm^{-3}$), φ ion fluence, and $^{Vac}/_{ion(Å)}$ is the vacancy per ion from SRIM 2013 [3].

Figure 6.1 shows the simulated relative atomic ratios of Ag and He implanted into SiC together with their simulated dpa as a function of depth in nm. Silver and helium have a maximum concentration of 2.8 % and 12 % at projected range 120 and 130 nm below the surface, respectively. What is also evident from figure 6.1 is that the profiles of Ag and He overlap, which makes a synergistic effect possible. Silver ions retain a maximum displacement of 60 dpa at a depth of 90 nm, while helium ions retain a maximum displacement of 5.3 dpa at 110 nm below the surface. The total displacement per atom for the co-implanted ions is 65 dpa at a depth of 90 nm below the surface. From these simulation results, it is quite clear that both individual implantations and co-implantation retain dpa that are greater than 0.3dpa (the critical amorphization of SiC) [4]. However, taking into consideration that implantation of both ions was done at 350 °C, which is well above the critical amorphization temperature of about 300 °C, the SiC structure is not expected to be amorphized [5].
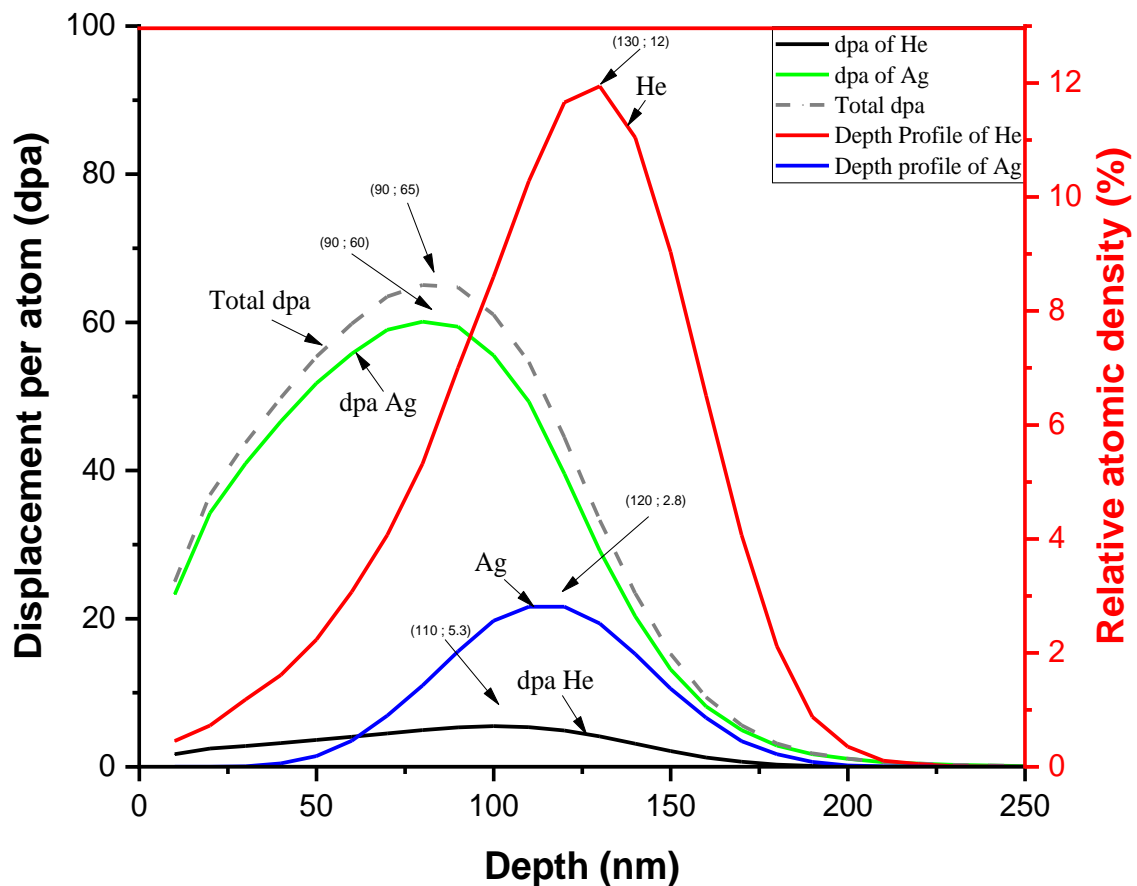

Figure 6. 1: Simulated results of Ag (360 keV) ions and He (17 keV) ions implanted into SiC.

6.2 Ag implants

6.2.1 Raman results

Figure 6.2 shows the Raman spectra of Ag implanted SiC, before and after annealing at temperatures ranging from 1000 °C to 1300 °C in steps of 100 °C for 5 hours. The Raman spectrum of un-implanted SiC is included for comparison in figure 6.2. Raman spectrum of un-implanted SiC has peaks at 799 cm^{-1} and 972 cm^{-1} correlating to transverse optical (TO) and longitudinal optical (LO) phonon modes of cubic 3C-SiC. The TO mode has a shoulder at 772 cm^{-1} indicating the presence of some hexagonal 6H-SiC polytype in the SiC substrate [6]. Thus, the polycrystalline SiC used in this work consists mainly of the cubic (3C-SiC) with some hexagonal (6H-SiC) present [7]. Also visible in figure 6.2 are the broad peaks at 1523 cm^{-1} and 1721 cm^{-1}, which are indicative of longitudinal optical overtones [8]. After implantation, there is a reduction in the intensity and broadness of the Raman characteristic peaks, indicating accumulation of defects without amorphization as initially predicted by the SRIM simulation results [9]. Isochronal annealing of the as-implanted samples resulted in the increase in the intensity of the characteristic SiC peaks indicating healing or annealing out of defects.

Since Raman peak parameters such as intensity, FWHM, and shift are affected by the crystal structure. Defects can lower the area of the undisturbed region, thus altering the distance between unit cells in a crystal lattice and crystal size [10]. Therefore radiation damage can be identified by the number of scattering molecules irradiated by the incident laser in Raman spectroscopy [11, 12]. The longitudinal optical mode can assist in detecting defects [13]. The recrystallization process after isochronal annealing (in this study) is based on the measurements of the peak position and the full width at half maximum of the LO mode. Figure 6.3 shows the peak position and FWHM of the LO mode from polycrystalline SiC as a function of temperature. There are no significant differences in Raman peak position, as depicted in figure 6.3. This means that for most atoms, the atomic distances did not change. Annealing at 1000 °C resulted in a decrease in FWHM compared to Ag as-implanted sample (14.2 cm^{-1}). This suggests that annealing at 1000 °C healed some of the defects, thus resulting in recrystallization of the SiC structure [7]. The FWHM progressively decreased with increasing annealing temperature up to 1300 °C. Figure 6.3 also shows that the FWHM after annealing at 1300 °C (11.8 cm^{-1}) is slightly more than that of the virgin (11.5cm^{-1}) sample indicating some defects are still remaining after annealing at this temperature [14].
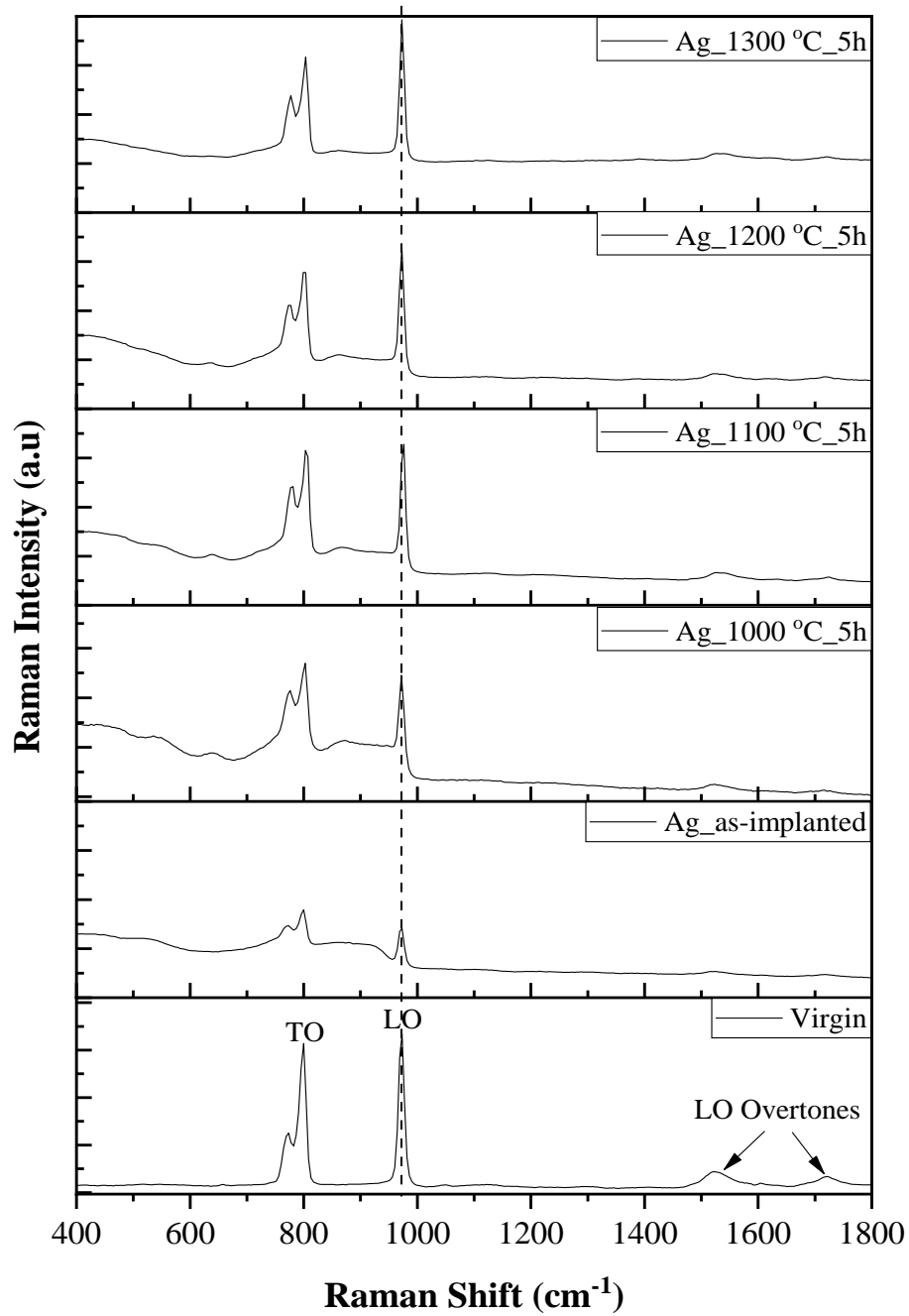
Figure 6. 2: Raman spectra of un-implanted SiC and Ag implanted into polycrystalline SiC before and after annealing from temperatures 1000 °C to 1300 °C for 5 hours.
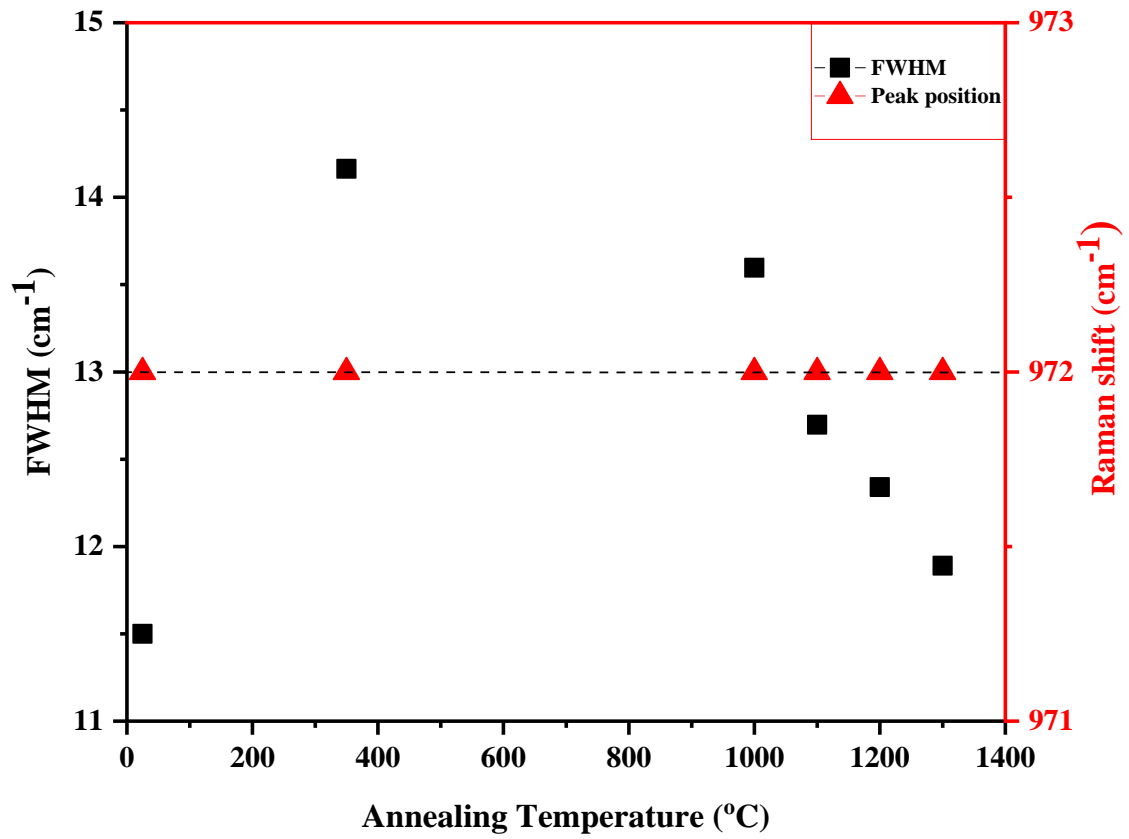
Figure 6. 3: The FWHM and the peak position of the LO mode as a function of temperature, before and after annealing from temperatures 1000 °C to 1300 °C for 5 hours.

6.2.2 Surface morphology results (SEM)

Figure 6.4 shows the SEM micrographs of Ag implanted samples before and after annealing. The SEM micrograph of a SiC virgin is flat with polishing marks. The polishing marks are due to polishing or cleaning hard surfaces during the manufacturing process [7]. These polishing marks are less visible in the as-implanted micrograph due to sputtering of the surface by impact ions [14]. The lower visibility of polishing marks indicate the presence of defects and lack of amorphization, which is consistent with the Raman results [15]. Annealing at 1000 °C caused no apparent morphological changes compared to the as-implanted sample indicating out of defects at this temperature. The grains and their boundaries became visible, with polishing marks still present after annealing at 1100 °C. Annealing at 1200 °C and 1300 °C resulted in grain boundaries becoming even more prominent. Moreover, higher temperatures annealing resulted in the formation of sub-grains inside the larger grains. The coarsening visible in figure 6.4(e) causes the reduction of sub-grain and hence clear grain boundaries [16]. Pore opening also took place after annealing at 1200 °C and 1300 °C. This opening might be due to thermal etching that is more preferred along the grain boundaries [17].
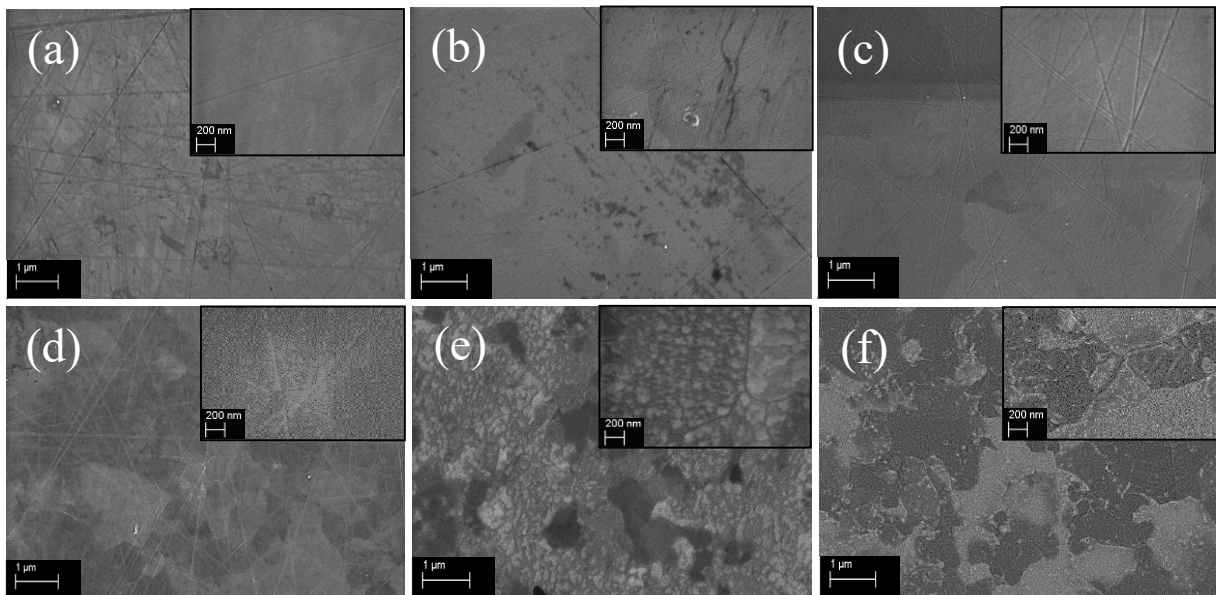

Figure 6. 4: SEM micrographs of SiC before and after implantation (a) SiC Virgin; (b) Ag-SiC as-implanted; (c) Ag-SiC_1000 °C_5h; (d) Ag-SiC_1100 °C_5h; (e) Ag-SiC_1200 °C_5h; (f) Ag-SiC_1300 °C_5h.

6.3 Ag and He implants

6.3.1 Raman results

Using Raman spectroscopy, the structural changes in Ag and He co-implanted samples before and after annealing were monitored. Figure 6.5 compares the Raman spectra obtained from un-implanted and co-implanted (Ag & He) SiC samples before and after annealing from temperatures of 1000 °C to 1300 °C for 5 hours. Raman spectrum of the un-implanted sample shows the Raman characteristic peaks of a polycrystalline SiC, as reported in section 6.2.1. Co-implantation of Ag and He resulted in the reduction of SiC Raman characteristic peaks intensity accompanied by broadening of LO peak, merging of TO peaks and appearance of Si-Si and C-C peaks around 531 and 1350 cm^{-1}. These indicate accumulation of severe defects without complete amorphization. From these results, it is quite clear that co-implantation retained more defects than Ag individual implantation which is in agreement with the simulated results that indicated more damage in the co-implanted samples (65 dpa) than the Ag only implanted sample (60 dpa). The more defects in the co-implanted samples might be due to accumulation of defects produced by two successive implanted ions which resulted in a higher defect concentration or more complex defects [7].

Similar to the Ag implanted sample the structural evolution after annealing was monitored by changes in the FWHM and the shift of the LO mode. Figure 6.6 shows the FWHM and peak position as a function of annealing temperature. The FWHM of the co-implanted sample broadened to about 17.4 cm^{-1} compared to virgin FWHM of 11.5 cm^{-1} indicating accumulation of defects. Annealing at 1000 °C resulted in the narrowing of the LO peak to about 13.4 cm^{-1} indicating annealing out of defects. Isochronal annealing at other higher temperatures resulted in a progressive reduction of the FWHM of the LO peak indicating progressive annealing of defects. The FWHM of the sample annealed at 1300 °C isn't exactly equal to that of FWHM of the un-implanted sample, indicating that some defects are still present [14]. No change was observed in LO peak position after either co-implantation or annealing. Thus, atomic distances essentially did not change for the majority of atoms. As a result of the annealing at 1000 °C, the D and G carbon peaks were visible. This suggests that the presence of He ion caused the graphitization of carbon in the SiC structure [18]. Increasing annealing temperature up to 1300 °C resulted in more pronounced carbon peaks.

The FWHM of the Ag+He as-implanted (17.4 cm^{-1}) is broader than the FWHM of Ag as-implanted (14.2 cm^{-1}). This implies that the structure of the co-implanted samples has significantly more defects, which is in agreement with the SRIM results and Raman spectra. In

both the Ag+He and Ag samples, annealing at 1000 °C narrows the FWHM, but the change is more pronounced in the co-implanted sample indicating that He enhances recrystallization. Isochronal annealing at higher temperatures resulted in progressive reduction in FWHM to approximately the same FWHM of the virgin sample. This further points to the effect of He in the recrystallization of SiC. Similar He enhanced recrystallization has been reported for SiC co-implanted with Mg and He annealed at 1573K [19].
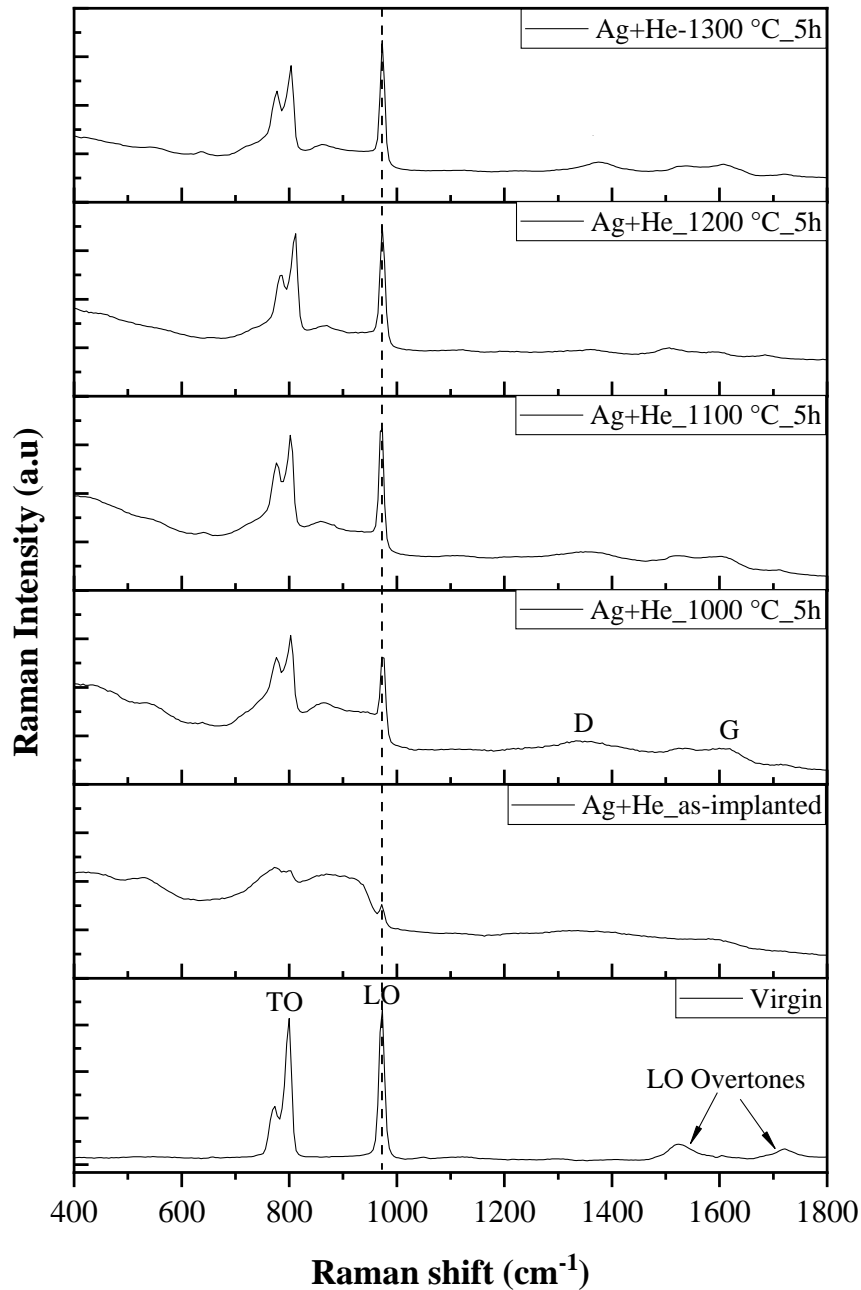

Figure 6. 5: Raman spectra of pristine SiC and Ag+He as-implanted SiC before and after annealing from temperatures 1000 °C to 1300 °C for 5 hours.
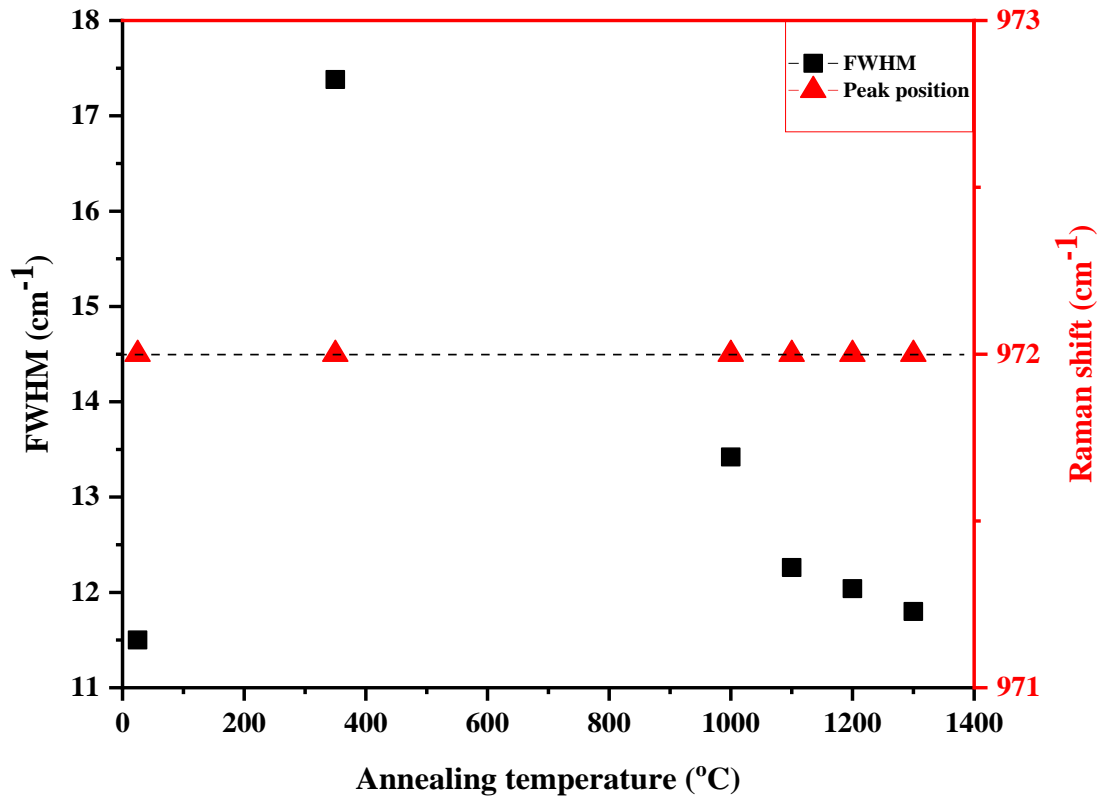
Figure 6. 6: The FWHM and the peak position of the LO mode as a function of temperature, before and after annealing from temperatures 1000 °C to 1300 °C for 5 hours.

6.3.2 Surface morphology results (SEM)

Figure 6.7 shows the SEM micrographs of the un-implanted and co-implanted samples before and after annealing. The un-implanted SiC have polishing marks on the surface [7], as reported in section 6.2.2. The SEM micrograph of the as-implanted sample has darker round structures and a few bright irregular shaped structures. The darker structures vary in size, with the smaller structures evenly distributed between the large dark structures and the bright structures. The higher magnification insert suggests that the darker structures are spherical and are protruding from the surface. The spheres might be blisters caused by helium molecules pushing up on the surface [20, 21]. Darker structures might be the holes resulting from the exfoliation of the blisters [22]. The sample annealed at 1000 °C contains some polishing marks and bright structures on the surface. Annealing at 1000 °C and 1100 °C increased the size of bright structures and reduced the size of dark structures at 1100 ° C. The number of bright structures increased with the increasing annealing temperature out to 1300 °C. Higher magnification inserts show that the polishing marks are still present in all samples but reduce with increasing annealing temperatures. The annealed at 1300 °C sample also contains slightly protruding spheres between the bright spots but are not dark as in the as-implanted, hence even barely visible.

To further investigate whether these features on the co-implanted samples are blisters and holes, the atomic force microscopy was used to analyse the surface topography of the co-implanted samples before and after annealing.
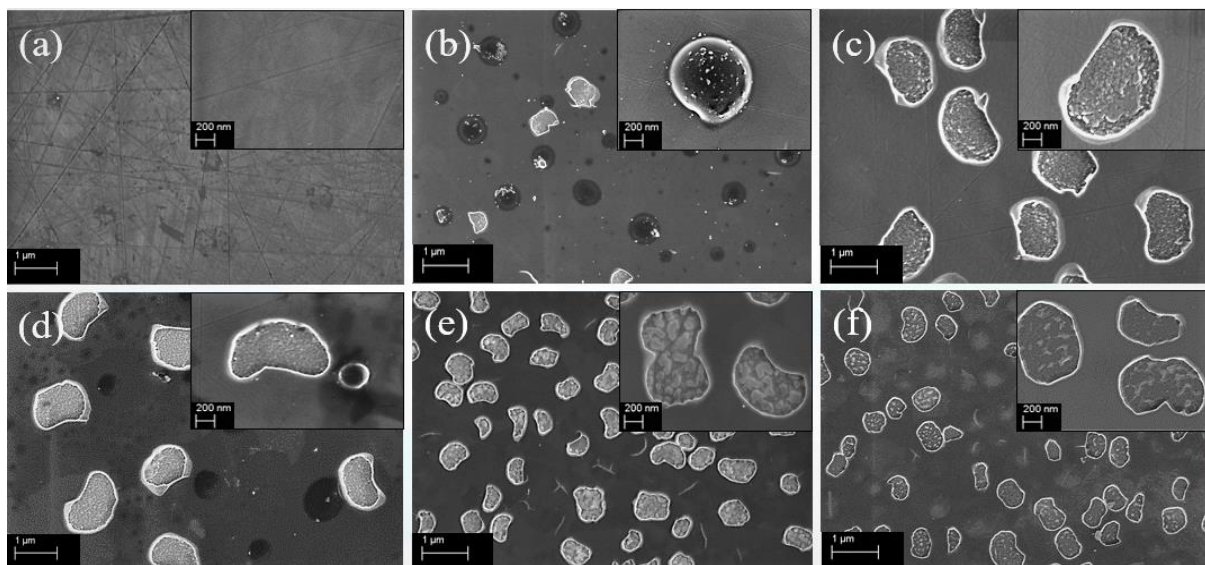

Figure 6. 7: SEM micrographs of SiC before and after implantation (a) SiC Virgin; (b) Ag+He-SiC as-implanted; (c) Ag+He-SiC_1000 °C_5h; (d) Ag+He-SiC_1100 °C_5h; (e) Ag+He-SiC_1200 °C_5h; (f) Ag+He-SiC_1300 °C_5h.

6.3.3 Atomic force microscopy (AFM) results

The surface morphology of the co-implanted samples before and after annealing were investigated using atomic force microscopy (AFM). Figure 6.8 shows the AFM images of the as-implanted and annealed samples together with their corresponding line profiles. All the AFM micrographs have bright and darker areas on their surfaces. Bright areas indicate topographical height and darker areas indicate topographical depths. The bright areas on the surface are blisters caused by helium bubbles inside SiC. During implantation of silver, energetic ions displace atoms out of their lattice sites, resulting in vacancies and displaced atoms in the interstitials. He ions penetrate through the damage caused by the first implantation (Ag ions), resulting in increased interstitials and vacancies. Since helium is inert, it tends to get trapped and cluster up in vacancies and thus creating extended defects [20]. The nucleation of helium in vacancies causes the formation of bubbles filled with helium molecules resulting in surface blistering [21]. Due to implantation at high temperatures, free helium (in interstitials) diffuses into vacancies forming high pressurized He blisters. As internal pressure builds up in these blisters, they exfoliate the surface, causing holes to form [22].

Annealing at a temperature of 1000 °C resulted in a high proportion of exfoliated blisters, with few blisters still present. Annealing at higher temperatures caused the exfoliation of more blisters resulting in holes on the surfaces. Upon reaching a critical size, blisters burst up to form holes in the SiC matrix due to the high-stress concentration [23]. The as-implanted line scan demonstrates the topographical height of He bubbles, which extend up to 53 nm, and the topographical depth of holes, which extend up to 122.5 nm. Between the large He blisters and holes, there is also evidence of smaller blisters. Annealing at 1000 °C increased the average diameter of the large He bubbles from 2.3 um to 2.7 um, while annealing at 1100 °C resulted in deeper holes. During annealing, vacancies migrate and merge with other vacancies resulting in larger blisters since He bubbles form in vacancies [18]. However, the size of the large blisters reduced with increasing annealing temperatures. This is because, at higher temperatures, the internal pressure in secondary bubbles of He is increased, which causes them to push up on the surface and form larger bubbles [22].
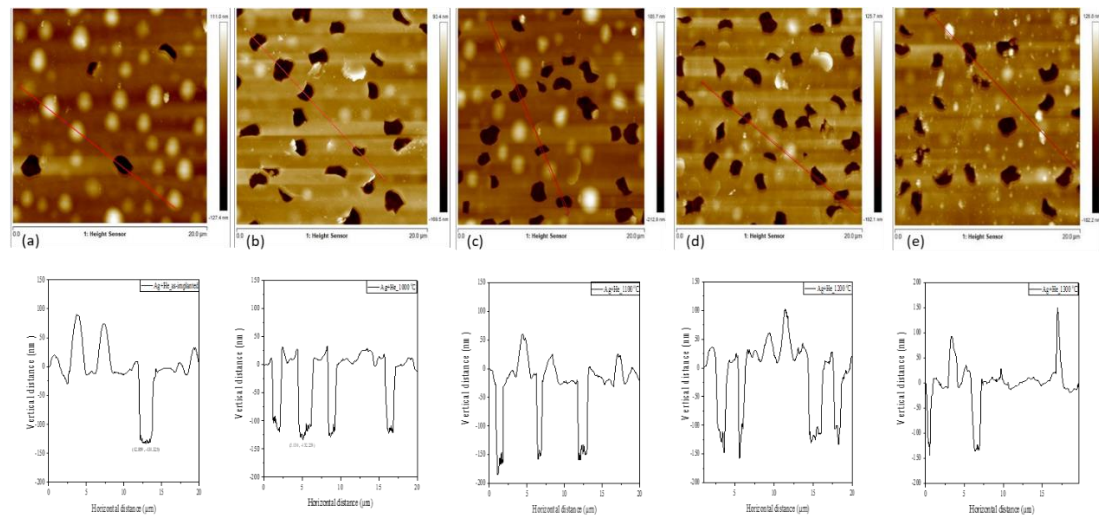
Figure 6. 8: AFM two-dimensional micrographs and line scans of SiC samples before (a) As-implanted and after annealing at (b) 1000 ^{o}C, (c) 1100 ^{o}C, (d) 1200 ^{o}C, and (e) 1300 ^{o}C.

6.4 Depth profile (ERDA) results of the Ag implanted and co-implanted (Ag + He) into SiC

In this study, ERDA was used to monitor the migration behaviour of Ag in the presence of He. ERDA has more advantages than RBS as it can detect both Ag and He [24]. Figure 6.9 shows the Time of Flight–Energy scatter plots of Ag implanted and Ag + He implanted then annealed at 1100 °C for 5 hours. The expected elements (He, Si, C, and Ag) are indicated in figure 6.9 as they are separated by their masses [25]. The samples also contain surface oxygen, possibly due to contamination of the surface of SiC [18]. The detected Au ion beam used for analysis is unmarked in figure 6.9. In figure 6.10, there is less concentration of Ag ions in the centre of the silver energy range after annealing. The annealed co-implanted sample has an even lesser concentration of Ag ions detected at that energy range, and the mass line is slightly longer (as can be seen in fig. 6.10(b)). This could mean that annealing resulted in ions being evenly dispersed in a larger energy range. After annealing, the mass line of He also shows less concentration of ions in the energy range of He.

The corresponding elemental depth profiles in figure 6.11 were calculated from ToF-E spectra using a density of 3.21 g.cm^{-3} [26]. The concentration of Ag as-implanted in the co-implanted sample is less than the concentration of Ag as-implanted in the single implanted sample. This implies that the implantation of He resulted in the out diffusion of implanted Ag accompanied by a substantial loss from the surface. Annealing at 1100 °C resulted in the out diffusion of He accompanied by loss He from the surface. However, no migration of Ag was observed in the

co-implanted sample after annealing at 1100 °C. Neither migration nor loss of implanted Ag were observed after annealing the Ag implanted samples at 1100 °C.

These results clearly demonstrate that He has a role in the retainment of Ag. The role of He in the migration of implanted Ag can be summarized as follows: He bubbles (as can be seen in the AFM micrographs of the un-annealed co-implanted sample) in the co-implanted samples cause the migration of Ag towards the surface (or the more defective region as seen from the SRIM results) accompanied by loss. Annealing at 1100 °C resulted in the out migration of He leaving cavities accompanied by no migration of Ag. The lack of Ag migration might indicate that Ag is trapped in the cavities. No migration of Ag was observed in the Ag only implanted sample annealed at 1100 °C. Therefore, He bubbles enhance the migration of Ag while He cavities are retards of the migration of Ag. These are important results for the application of SiC in both fission and fusion reactor environments. However, most investigations need to be done especially at an atomic level to clear understand the role of He in the migration of Ag.
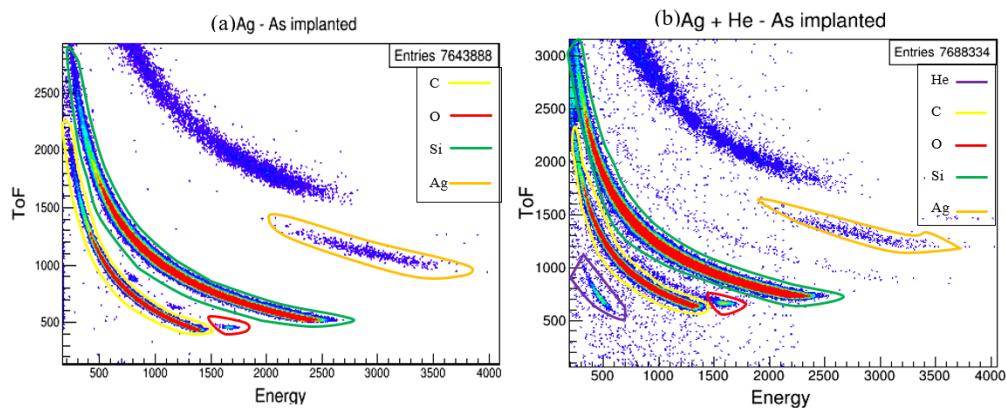

Figure 6. 9: Two-dimensional Time of Flight–Energy plots showing recoil ions from as-implanted (a) Ag –SiC and (b) He & Ag–SiC samples bombarded by 30 MeV Au ions.
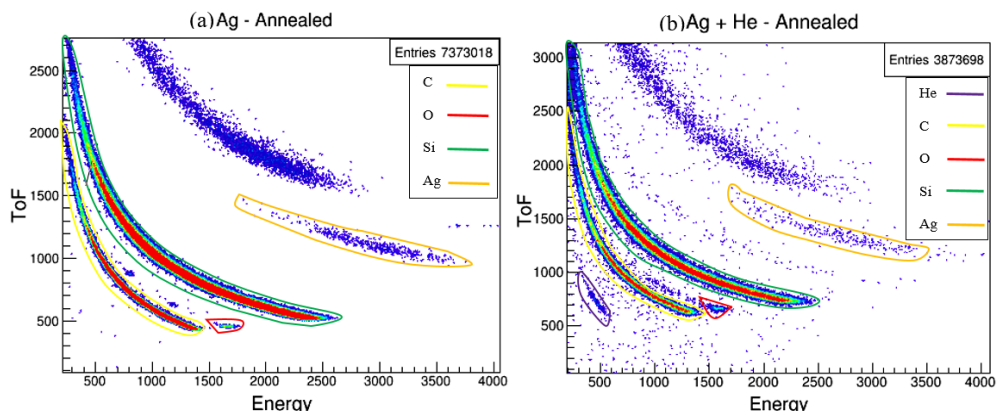

Figure 6. 10: Two-dimensional Time of Flight–Energy plots showing recoil ions from annealed at 1100 °C (a) Ag –SiC and (b) He & Ag–SiC samples bombarded by 30 MeV Au ions.
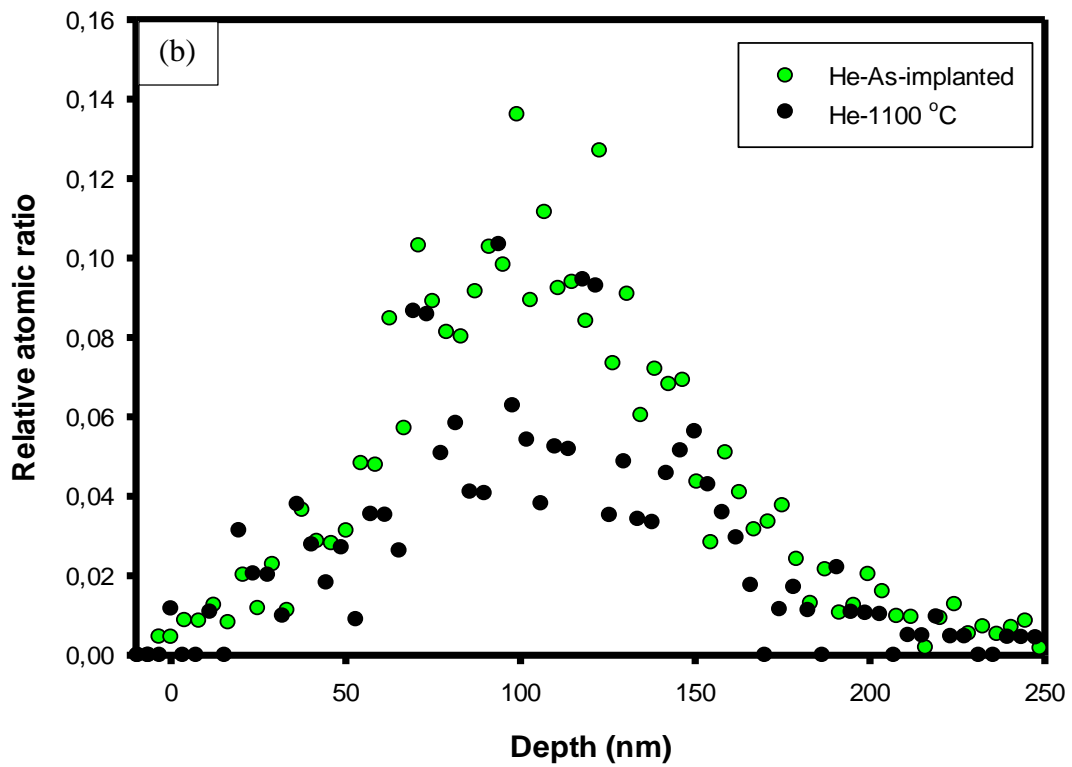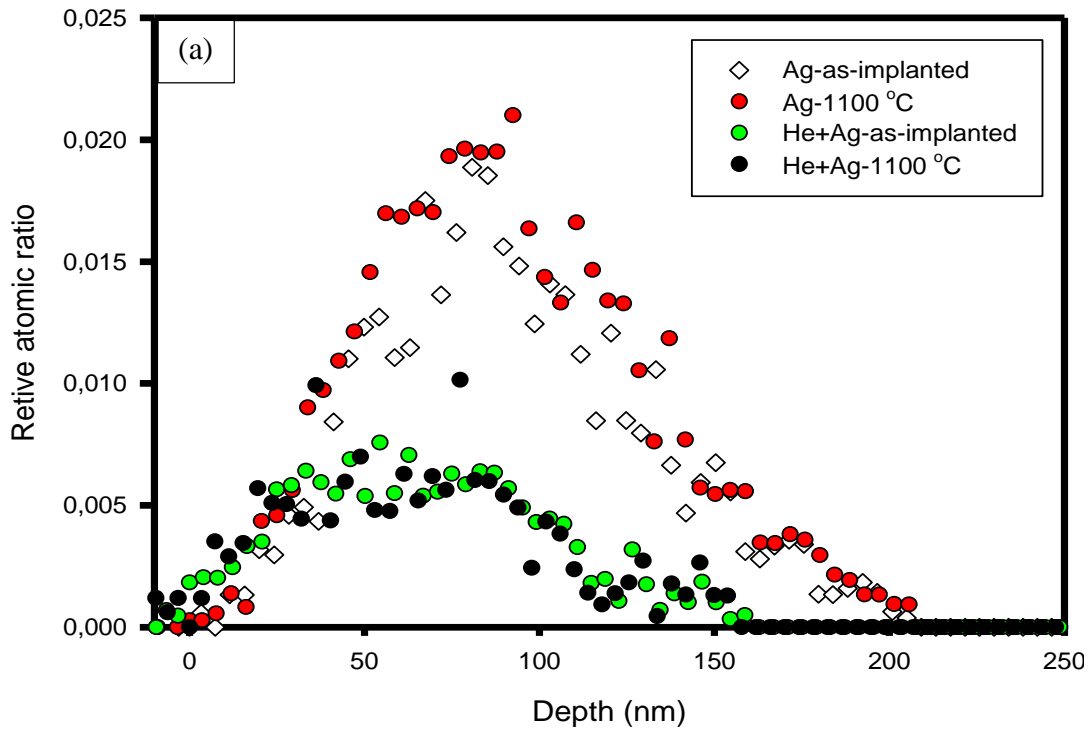
Figure 6. 11: Elastic recoil detection analysis (ERDA) profiles of (a) Ag and (b) He before and after annealing at 1100 °C for 5 hours.

References

1. R. Devanathan, and W. J. Weber, 2000, Displacement energy surface in 3C and 6H SiC, Journal of nuclear materials, 278(2-3), pp. 258-265.

2. T. T. Hlatshwayo, L. D. Sebitla, E. G. Njoroge, M. Mlambo, and J. B. Malherbe, 2017, Annealing effects on the migration of ion-implanted cadmium in glassy carbon, Nuclear Instruments and Methods in Physics Research Section B: Beam Interactions with Materials and Atoms, 395, pp. 34-38.

3. J. F. Ziegler, M. D. Ziegler, and J. P. Biersack, 2010, SRIM–The stopping and range of ions in matter (2010), Nuclear Instruments and Methods in Physics Research Section B: Beam Interactions with Materials and Atoms, 268(11-12), pp. 1818-1823.

4. C. J. McHargue, and J. M. Williams, 1993, Ion implantation effects in silicon carbide, Nuclear Instruments and Methods in Physics Research Section B: Beam Interactions with Materials and Atoms, 80, pp.889-894.

5. W. J. Weber, L. M. Wang, N. Yu, and N. J. Hess, 1998, Structure and properties of ion-beam-modified (6H) silicon carbide, Materials Science and Engineering: A, 253(1-2), pp. 62-70.

6. J. Wasyluk, T.S. Perova, S.A. Kukushkin, A.V. Osipov, N.A. Feoktistov, and S.A. Grudinkin, 2010, Raman investigation of different polytypes in SiC thin films grown by solid-gas phase epitaxy on Si (111) and 6H-SiC substrates, In Materials science forum (645, pp. 359-362), Trans Tech Publications Ltd.

7. T. T. Hlatshwayo, N. Mtshonisi, E.G. Njoroge, M. Mlambo, M. Msimanga, V.A. Skuratov, J. H. O'Connell, J. B. Malherbe, and S. V. Motloung, 2020, Effect of Ag and Sr dual implanted into SiC, Nuclear Instruments and Methods in Physics Research Section B: Beam Interactions with Materials and Atoms, 472, pp. 7-13.

8. X. Feng, and Y. Zang, 2016, Raman scattering properties of structural defects in SiC, In 2016 3rd International Conference on Mechatronics and Information Technology, Atlantis Press.

9. J.B. Malherbe, 2013, Diffusion of fission products and radiation damage in SiC, Journal of Physics D: Applied Physics, 46(47), pp. 473001.

10. N. Daghbouj, B.S. Li, M. Callisti, H.S. Sen, J. Lin, X. Ou, M. Karlik, and T. Polcar, 2020, The structural evolution of light-ion implanted 6H-SiC single crystal: Comparison of the effect of helium and hydrogen, Acta Materialia, 188, pp. 609-622.

11. Z. Xu, Z. He, Y. Song, X. Fu, M. Rommel, X. Luo, A. Hartmaier, J. Zhang, and F. Fang, 2018, Topic review: Application of raman spectroscopy characterization in micro/nano-machining, Micromachines, 9(7), pp. 361.

12. S. Sorieul, J. M. Costantini, L. Gosmain, L. Thomé, and J. J. Grob, 2006, Raman spectroscopy study of heavy-ion-irradiated α-SiC, Journal of Physics: Condensed Matter, 18(22), p.5235.

13. G. Litrico, N. Piluso, and F. La Via, 2017, Detection of crystallographic defects in 3C-SiC by micro-Raman and micro-PL analysis, In Materials Science Forum (897, pp. 303-306), Trans Tech Publications Ltd.

14. Z. A. Y. Abdalla, M. Y. A. Ismail, E. G. Njoroge, T. T. Hlatshwayo, E. Wendler, and J. B. Malherbe, 2020, Migration behaviour of selenium implanted into polycrystalline 3C–SiC, Vacuum, 175, pp. 109235.

15. J. B. Malherbe, N. G. van der Berg, A. J. Botha, E. Friedland, T. T. Hlatshwayo, R. J. Kuhudzai, E. Wendler, W. Wesch, P. Chakraborty, and E. F. Da Silveira, 2013, SEM Analysis of Ion Implanted SiC, Nuclear Instruments and Methods in Physics Research Section B: Beam Interactions with Materials and Atoms, 315, pp. 136-141.

16. H. Sheng, Z. Sun, I. Uytdenhouwen, G. Van Oost, and J. Vleugels, 2015, Temperature and deformation effect on the low and high angle grain boundary structure of a double forged pure tungsten, International Journal of Refractory Metals and Hard Materials, 50, pp. 184-190.

17. T. M. Mohlala, J. B. Malherbe, and T. T. Hlatshwayo, 2020, Effect of radiation damage on the migration behaviour of europium implanted into polycrystalline SiC at RT, 350° C and 600° C, Nuclear Instruments and Methods in Physics Research Section B, 478, pp. 260-268.

18. T. T. Hlatshwayo, C. E. Maepa, M. Msimanga, M. Mlambo, E. G. Njoroge, V. A. Skuratov, S. V. Motloung, and J. B. Malherbe, 2021, Helium assisted migration of silver implanted into SiC, Vacuum, 183, pp. 109865.

19. M. Liu, H. Gong, W. Liu, R. Liu, and J. Cao, 2021, Effects of He on the recrystallization and Mg diffusion in Mg ion implanted CVD-SiC, Journal of Nuclear Materials, 545, pp. 152747.

20. N. Daghbouj, J. Lin, H. S. Sen, M. Callisti, B. Li, M. Karlik, T. Polcar, Z. Shen, M. Zhou, T. You, and X. Ou, 2021, Blister formation in He-H co-implanted InP: A comprehensive atomistic study, Applied Surface Science, 552, pp. 149426.

21. B. S. Li, Z. G. Wang, and H. P. Zhang, 2015, Study of surface blistering in GaN by hydrogen implantation at elevated temperatures, Thin Solid Films, 590, pp. 64-70.

22. N. Daghbouj, B.S. Li, M. Karlik, and A. Declemy, 2019, 6H-SiC blistering efficiency as a function of the hydrogen implantation fluence, Applied surface science, 466, pp. 141-150.

23. Q. Shen, G. Ran, W. Zhou, C. Ye, Q. Feng, and N. Li, 2018, Investigation of surface morphology of 6H-SiC irradiated with He^+ and H^{2+} ions, Materials, 11(2), pp. 282.

24. J. L'ecuyer, C. Brassard, C. Cardinal, J. Chabbal, L. Deschenes, J. P. Labrie, B. Terreault, J. G. Martel, and R. St.-Jacques, 1976, An accurate and sensitive method for the determination of the depth distribution of light elements in heavy materials, Journal of Applied Physics, 47(1), pp. 381-382.

25. S. Khamlich, M. Msimanga, C. A. Pineda-Vargas, Z. Y. Nuru, R. McCrindle, and M. Maaza, 2012, Compositional analysis and depth profiling of thin film CrO2 by heavy ion ERDA and standard RBS: a comparison, Materials characterization, 70, pp. 42-47.

26. P. Trocellier, and T. Sajavaara, (2006), Elastic recoil detection analysis. Encyclopedia of Analytical Chemistry: Applications, Theory and Instrumentation, John Wiley and Sons Ltd, Chichester, United Kingdom.

CHAPTER 7

CONCLUSION AND FUTURE STUDIES

In this study, helium and silver ions were co-implanted into polycrystalline silicon carbide at 350 °C to examine the structural evolution of SiC and the migration behavior of Ag in the presence of He. 360 keV Ag ions were implanted into polycrystalline SiC at 350 °C to a fluence of 2×10^{16} cm^{-2}. Some Ag implanted samples were then implanted with 17 keV He ions to a fluence of 1×10^{17} cm^{-2} at 350 °C. The samples were then annealed at temperatures ranging from 1000 °C to 1300 °C in steps of 100 °C for 5 hours. Raman spectroscopy was used to determine the structural changes, scanning electron microscopy (SEM) to determine the morphologic changes, and atomic force microscopy (AFM) to determine changes in the surface topography of the samples. The elemental depth profiles of the implanted species were monitored using Elastic Recoil Detection Analysis (ERDA).

Raman results showed that implanting at 350 °C led to the accumulation of defects, and co-implantation retained more defects without amorphization. There was more damage in the co-implanted sample because of the interaction of defects produced by two successive implanted ions, which resulted in a higher defect concentration. Isochronal annealing of the as-implanted samples resulted in healing or annealing out of defects, which resulted in the recovery of the SiC crystal structure. The recovery process progressively increased with increasing annealing temperature up to 1300 °C. Annealing at 1300 °C almost completely restored the entire crystal structure, with co-implanted samples recovering faster than individually implanted samples. Therefore, the implanted He assisted in the recrystallization of the SiC. In agreement with the SRIM simulation and Raman results, less visible polishing marks were observed in the SEM micrographs of both as-implanted samples (both individual and co-implanted). Annealing at high temperatures resulted in the appearance of grains and their boundaries, and the grain boundaries became more prominent with increasing annealing temperature. AFM micrographs revealed that co-implantation of Ag and He led to the formation of blisters and holes on the surface indicating the formation of bubbles accompanied by exfoliation of the surface during co-implantation. Annealing at high temperatures resulted in the severe exfoliation of the surface resulting in more holes on the surfaces. The ERDA profiles indicated that the helium implantation resulted in the out-diffusion of implanted Ag resulting in a considerable loss from the surface. Annealing at 1100 °C resulted in the out-migration of He accompanied by no

migration of Ag. No migration of Ag was observed in the Ag only implanted sample annealed at 1100 °C. Since He bubbles are formed in vacancies in the co-implanted SiC, the out-migration of He is expected to leave cavities in the implanted layer. Therefore, results suggest that He bubbles in the co-implanted samples cause the migration of Ag towards the surface resulting in the loss while the cavities in the implanted layers are responsible of trapping implanted Ag.

These results are highly relevant in a nuclear environment where SiC is exposed to various fission products at high temperatures in the presence of He. However, to get more insight in the migration of Ag in the presence of He bubbles. Similar investigation should be done at an atomic scale using transmission electron microscopy (TEM) and in the presence of other ions that are present in during nuclear reactor operation such as swift heavy ions (SHIs).